

**DEVELOPMENT OF MILLIMETER WAVE
INTEGRATED-CIRCUIT INTERFEROMETRIC SENSORS
FOR INDUSTRIAL SENSING APPLICATIONS**

A Dissertation

by

SEOKTAE KIM

Submitted to the Office of Graduate Studies of
Texas A&M University
in partial fulfillment of the requirements for the degree of

DOCTOR OF PHILOSOPHY

December 2004

Major Subject: Electrical Engineering

UMI Number: 3202250



UMI Microform 3202250

Copyright 2006 by ProQuest Information and Learning Company.
All rights reserved. This microform edition is protected against
unauthorized copying under Title 17, United States Code.

ProQuest Information and Learning Company
300 North Zeeb Road
P.O. Box 1346
Ann Arbor, MI 48106-1346

**DEVELOPMENT OF MILLIMETER WAVE
INTEGRATED-CIRCUIT INTERFEROMETRIC SENSORS
FOR INDUSTRIAL SENSING APPLICATIONS**

A Dissertation

by

SEOKTAE KIM

Submitted to Texas A&M University
in partial fulfillment of the requirements
for the degree of

DOCTOR OF PHILOSOPHY

Approved as to style and content by:

Cam Nguyen
(Chair of Committee)

Robert D. Nevels
(Member)

Chin B. Su
(Member)

Roger E. Smith
(Member)

Chanan Singh
(Head of Department)

December 2004

Major Subject: Electrical Engineering

ABSTRACT

Development of Millimeter Wave Integrated-Circuit Interferometric

Sensors for Industrial Sensing Applications. (December 2004)

Seoktae Kim, B.S., Inha University, S. Korea;

M.S., Pohang University of Science and Technology, S. Korea

Chair of Advisory Committee: Dr. Cam Nguyen

New millimeter wave interferometric, multifunctional sensors have been studied for industrial sensing applications: displacement measurement, liquid-level gauging and velocimetry. Two types of configuration were investigated to implement the sensor: homodyne and double-channel homodyne. Both sensors were integrated on planar structure using MMIC (Microwave Monolithic Integrated Circuit) and MIC (Microwave Integrated Circuit) technology for light, compact, and low-cost design. The displacement measurement results employing homodyne configuration show that sub-millimeter resolution in the order of 0.05 mm is feasible without correcting the non-linear phase response of the quadrature mixer.

The double-channel homodyne configuration is proposed to suppress the non-linearity of the quadrature mixer and to estimate the effect of frequency stability of a microwave signal source without the help of additional test equipment, at the loss of a slight increase of circuit complexity. The digital quadrature mixer is constituted by a quadrature-sampling signal processing technique and takes an important role in the elimination of conventional quadrature mixer's nonlinear phase response. Also, in the same displacement measurement, the radar sensor with the double-channel homodyne configuration provided a better resolution of 0.01mm, the best-reported resolution to date in terms of wavelength in the millimeter wave range, than the sensor employing simple homodyne configuration.

Short-term stability of a microwave signal source, which is an important issue in phase sensitive measurement, is also considered through phase noise spectrum obtained by FFT spectral estimator at Intermediate Frequency (IF).

The developed sensors demonstrate that displacement sensing with micron resolution and accuracy and high-resolution low-velocity measurement are feasible using millimeter-wave interferometer, which is attractive not only for displacement and velocity measurement, but also for other industrial sensing applications requiring very fine resolution and accuracy.

To my parents and my wife

ACKNOWLEDGEMENTS

I would like to express my deepest gratitude to Dr. Nguyen for his advice and support throughout this research. I would like to also thank Dr. Nevels and Dr. Smith for serving as committee members and for helping me through my final steps. Special thanks are given to Dr. Su who was willing to provide me the use of the valuable microwave frequency synthesizer for my research.

I wish to acknowledge the donation of MMICs from TriQuint and Northrop Grumman, and the help on wire bonding process from Ratheon. I also have to express my gratitude to Dr. James Carroll for his assistance on MMIC.

Most of all, I am grateful to my wife, Hyunjeong Jung, for her encouragement and patience over the past six years.

This research was supported in part by the National Science Foundation and in part by the National Academy of Sciences.

TABLE OF CONTENTS

CHAPTER	Page
I INTRODUCTION	1
II ANALYSIS OF INTERFEROMETER	7
2.1 Interaction of electromagnetic wave with dielectric plate.....	7
2.2 Determination of relative dielectric constant and thickness.....	9
2.3 Signal analysis of microwave interferometer.....	11
III HOMODYNE INTERFEROMETRIC SENSOR	16
3.1 System configuration and principle.....	17
3.2 Phase unwrapping signal processing	20
3.3 System fabrication	23
3.4 Displacement measurement and liquid-level gauging.....	25
3.5 Error analysis contributed by quadrature mixer.....	29
3.5.1 Quadrature mixer transfer function.....	29
3.5.2 I/Q error correction algorithm.....	33
3.5.3 Worst-case error analysis.....	38
3.6 Summary.....	40
IV DOUBLE-CHANNEL HOMODYNE INTERFEROMETRIC SENSOR.....	41
4.1 System configuration and principle.....	44
4.1.1 Displacement measurement.....	46
4.1.2 Doppler velocimetry	48
4.2 Signal processing	48
4.2.1 Phase-difference detection for displacement measurement..	49
4.2.2 Doppler-frequency estimation for velocity measurement....	52
4.3 System fabrication and test.....	58
4.3.1 Displacement measurement results.....	61
4.3.2 Velocity measurement result.....	65
4.4 Summary.....	67

CHAPTER	Page
V CONSIDERATION OF FREQUENCY STABILITY OF MICROWAVE SIGNAL SOURCE.....	68
5.1 Theoretical analysis of phase-noise effect on interferometric measurements.....	68
5.2 Phase noise estimation.....	77
VI CONCLUSION	83
REFERENCES	86
VITA	92

LIST OF FIGURES

FIGURE	Page
1.1 Michelson interferometer.....	1
1.2 Typical schematic diagram of microwave interferometer	3
1.3 Microwave interferometer employing one antenna to measure reflected wave.....	4
1.4 Double-channel homodyne microwave interferometer.....	5
2.1 Geometry involved in the analysis.....	7
2.2 Phase of reflection coefficient depending on (a) relative dielectric constant (b) dielectric thickness.....	12
2.3 Phase of transmission coefficient depending on (a) relative dielectric constant (b) dielectric thickness.....	13
3.1 Overall system configuration	17
3.2 Original unwrapped, wrapped and reconstructed phase sequences	22
3.3 Millimeter wave circuit layout in detail	23
3.4 Photograph of the fabricated system	24
3.5 Measured signal voltage (a) and detected and constructed phase (b).....	26
3.6 Measured displacement for a metal plate	27
3.7 Measurement set-up for water level gauging (a) and test results (b).....	28
3.8 Functional block diagram of quadrature mixer	29
3.9 Example of non-linear phase response of quadrature mixer	31
3.10 Frequency response of ideal and real quadrature mixer	34

FIGURE	Page
3.11 I/Q error correction (a) I/Q channel response (b) Geometric interpretation of I/Q error correction.....	37
3.12 Constant ISR contours	39
4.1 Overall system block diagram. The target sits either on the XYZ axis (for displacement sensing) or on the conveyor (for velocity measurement). The Reference channel is not needed for velocity measurement.....	45
4.2 Signal processing flow in the digital signal processor for displacement measurement.....	49
4.3 Configuration of the digital quadrature mixer	51
4.4 Signal processing flow for velocity measurement	53
4.5 Linear regression for the Doppler frequency of ± 1 Hz	56
4.6 Time response of the DQM for the Doppler frequency of $+1$ Hz	56
4.7 Histogram of the estimated Doppler frequency using MLE and linear regression methods.....	57
4.8 Photograph of the fabricated millimeter-wave (a) and intermediate-signal (b) subsystems.....	59
4.9 Millimeter wave subsystem layout in detail	60
4.10 Measurement-channel response for every 100- μm displacement. Thick solid line represents reference-channel signal	61
4.11 Detected and unwrapped phase	63
4.12 Measured displacement and error for a metal plate	63
4.13 Error correction by the polynomial curve fitting	64
4.14 Displacement results after error correction	64

FIGURE	Page
4.15 Displacement measured every 10 μm	65
4.16 Velocity measurement result for a closing target	66
5.1 Schematic representing the operation of a typical homodyne interferometer.....	73
5.2 Calculated time delay effect on the frequency noise PSD	76
5.3 rms displacement error of millimeter-wave interferometer operating at 36-GHz.....	76
5.4 Phase-noise spectrum of each channel	77
5.5 Probability distribution function (a) and probability density function (b) for the phase difference.....	82

LIST OF TABLES

TABLE		Page
1	Comparison of the developed sensor's performance with those of commercial liquid-level gauging sensor	40

CHAPTER I

INTRODUCTION

In a wide sense, interferometry is a scientific technique, as it literally implies, to interfere or correlate two, or more than two, signals to form a physically observable measure, like a fringe pattern in optical interferometry, or electrical signals of power or voltage in most radio interferometry, from which any useful information can be inferred. The history of interferometry dates back to 1887 when American physicist A. A. Michelson first demonstrated optical interferometer experimentally to measure the speed of light, which later became the foundation of Einstein's Theory of Relativity. The basic building blocks of the Michelson interferometer, which is composed of a coherent light source, two mirrors, a beam splitter, and a detector, are shown in Fig. 1.1.

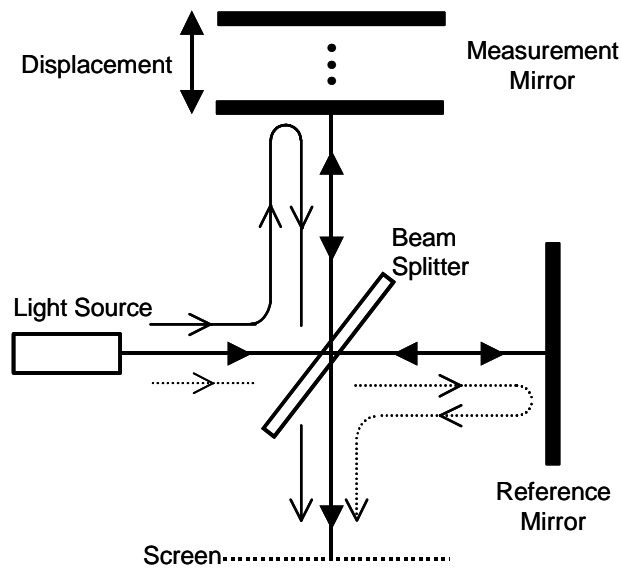


Fig. 1.1. Michelson interferometer.

The Michelson interferometer works on the principle that the coherent light wave split by the beam splitter forms constructive or destructive light intensity variation, interference fringe, according to the phase relationship between the two waves split when they are interfered. In the interferometer, the light source is divided into two waves. One is used as a reference wave, traveling the path that the dotted line arrow indicates in Fig. 1.1. The other serves as a measurement wave whose traveling path is depicted by the solid line arrow. Interfering two waves results in a fringe image that is used for interferometric measurement. Michelson later extended his experiment into the study of spectral lines, measurement of the standard meter, and even the measurement of the angular diameter of stars [1]. Since the first interferometer was devised, many different forms of interferometers have been investigated with different frequency sources. The advent of laser has played great role in the development of optical interferometry. Today, the interferometry applies to even medicine and biology [2]-[3], as well as various measurement techniques.

Although major achievements of interferometry originate from optical interferometry, radio interferometry, using spectrum in microwave or millimeter wave range, has been investigated enormously in areas such as radio astronomy and astrometry, plasma diagnostics, nondestructive material evaluation, and sensing applications. The radio interferometer has many similarities to radar in the aspects of structure and principle. The noticeable difference between them is that the radio interferometer is used mainly in laboratory or short distance, while radar is used for long distance applications. With this reason, the radio interferometer can be regarded as a kind of coherent radar in terms of radar terminology. As an example of the radio interferometer, Fig. 1.2 shows a typical schematic diagram of a microwave interferometer to measure electron density in a plasma chamber or to evaluate complex permittivity of a dielectric medium, located between the two antennas. The structure of the microwave interferometer shown in Fig. 1.2 is analogous to the Mach-Zehnder interferometer [4] used in optics, except for the microwave components used to build the system.

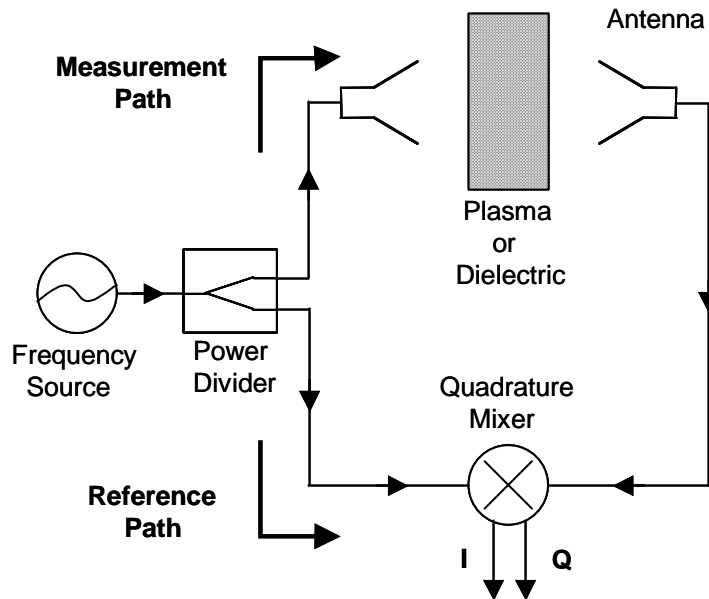


Fig. 1.2. Typical schematic diagram of microwave interferometer.

In the microwave interferometer depicted in Fig. 1.2, the power of the microwave or millimeter wave is divided by the power divider, which can also be replaced with a directional coupler or hybrid junction, to guide the wave into two paths, measurement and reference path. A dielectric medium with properties to be measured is placed in the measurement path. The wave in the measurement path carries information that one wants to measure, such as electron density of plasma or the material properties of dielectric, after passing through the medium. This wave then interferes with the wave in the reference path by means of the quadrature mixer, resulting in in-phase(I) and quadrature(Q) signals from which any physical quantity relating to the properties of dielectric is extracted. It is also possible to constitute interferometer employing only one antenna, as shown in Fig. 1.3, detecting the reflected wave instead of transmitted wave. In view of radar engineering, this is generally called a reflectometer or monostatic system. Due to its inherent versatilities, this type of system has been used for a wide range of applications and also adopted as a system topology in this research. In the system, a circulator is used to separate the reflected wave from the transmitted wave.

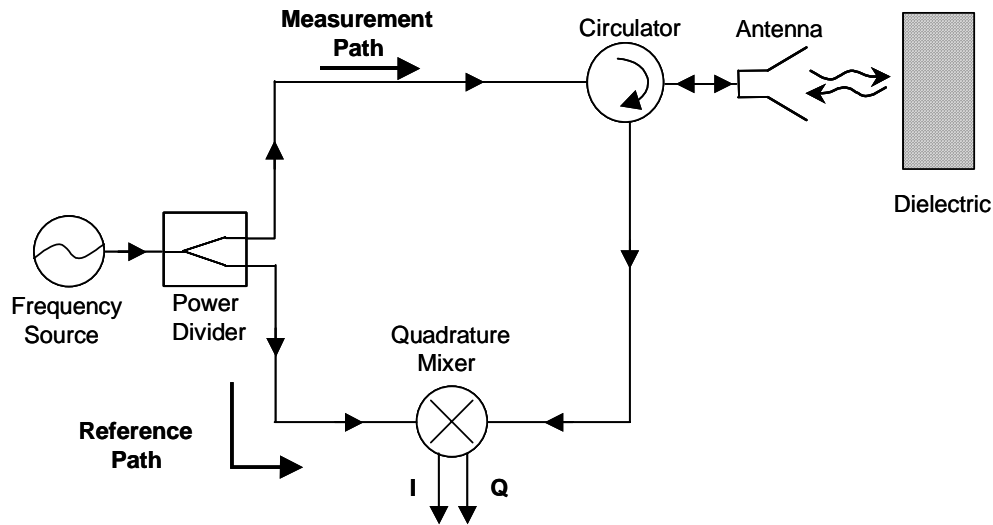


Fig. 1.3. Microwave interferometer employing one antenna to measure reflected wave.

Another form of interferometer is shown in Fig. 1.4 where either a reference or measurement wave is modulated by a quadrature upconverter to generate a single side band (SSB) signal which is slightly shifted in frequency by f_m with reference to the frequency f of the signal source. In this system, the output signal of the mixer is not DC or zero-IF, as previously discussed in the systems in Fig. 1.2 and Fig. 1.3. The measurement process is accomplished by comparing the phase of the modulating signal of frequency f_m to the output signal of the mixer that has a frequency of f_m and contains information on the material to be evaluated. In Fig. 1.4, the interferometer employing two antenna is illustrated as an example, but one antenna configuration is also possible. The main advantages of this topology are its ease in avoiding $1/f$ noise generated by the semiconductor components used, and elimination of I/Q error of the quadrature mixer, as explained in chapter III.

Optical interferometry, depending on the number of light sources used, is traditionally classified as a homodyne or heterodyne interferometer. Two waves interfered of different frequency, which comes from two different light sources, is generally called heterodyne in optical interferometry. Modern advances in optical

interferometry give rise to further classifications, besides the number of light sources, based on the parameters to describe the interferometers [4]-[5]. However, strict classifications are not found in radio interferometers. The nomenclature of homodyne and double-channel homodyne interferometric sensors is adopted throughout this dissertation, relying on the number of junctions to divide and combine the millimeter waves in the system, as proposed in [6].

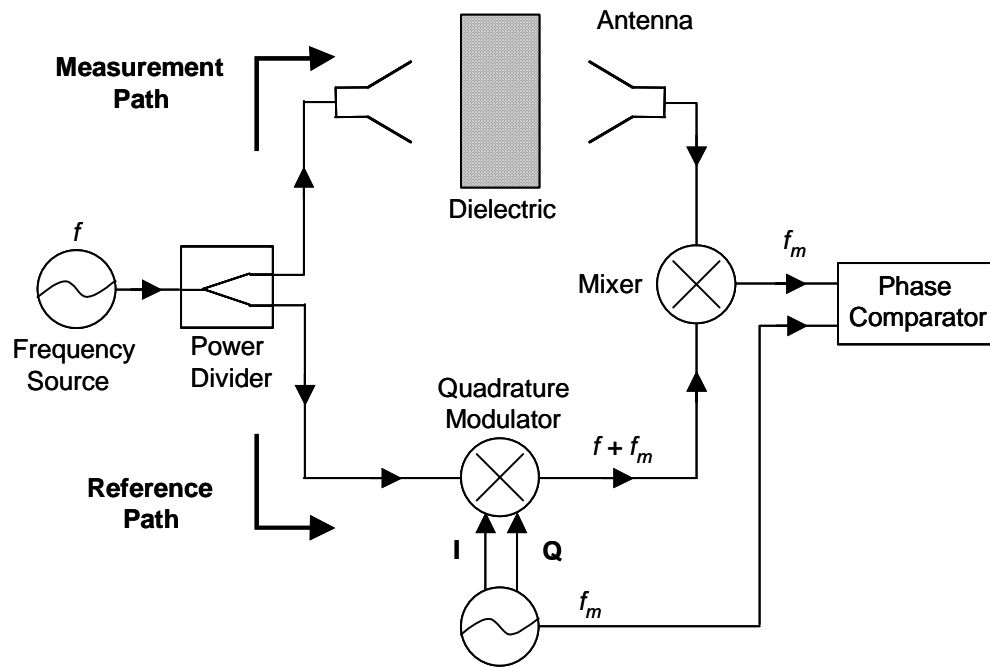


Fig. 1.4. Double-channel homodyne microwave interferometer.

Millimeter wave sensors have been widely investigated for industrial sensing applications due to growing demands of automation in production processes and process control, especially for hostile environments with high temperature, dust, smoke, and potential danger of explosion. Recently, millimeter wave radars have drawn much attention in automobile application, which has a huge potential market in the near future. Moreover, with the advances in high-speed solid-state electronics operating in millimeter wave frequency range, the sensors have been developed in a lighter, cheaper, and more

compact way than ever before. Those advances make it possible to design and implement the radar sensors in planar structure. It is the aim of this research to develop millimeter wave interferometric sensors using microwave integrated circuits (MICs) and microwave monolithic integrated circuits (MMICs) for commercial use. Much progress in millimeter wave sensors is found with pulse or FMCW (Frequency Modulated Continuous Wave) techniques. We aim to demonstrate that a millimeter-wave interferometric radar sensor operating at a single-frequency CW provides a more attractive solution than the pulse or FMCW radar sensor for short-range applications requiring high resolution and fast response.

We present the development of millimeter wave sensors, based on the interferometry principle, measuring displacement, liquid level gauging, and velocity for industrial sensing applications. From the viewpoint of radar and communication systems, the sensors developed are classified as simply homodyne or double-channel homodyne interferometric sensors. The dissertation is organized as follows: chapter II analyzes the principle of interferometry for exemplary study of relative dielectric constant and thickness derivation; chapter III is devoted to the sensor with homodyne system configuration incorporating displacement measurement and liquid level gauging; chapter IV describes the sensor with double-channel homodyne configuration for displacement and velocity sensing; chapter V includes the analysis of a phase noise effect on interferometric measurement; and, finally, analysis and suggestion for future research are given in chapter VI.

CHAPTER II

ANALYSIS OF INTERFEROMETER

In this chapter, the principle of microwave interferometry is investigated for the measurement of permittivity and thickness of the dielectric shown in Figs. 1.2, 1.3, and 1.4, as an exemplary study. It is shown that the permittivity and thickness of dielectric can be determined from the measured phase of reflection and transmission of plane electromagnetic waves reflected from or transmitted through the material. It should be noted that the same principle can be applied for general interferometric measurement, for example, displacement, distance and velocity measurements, by defining the relationship between the phase detected and any physical measure to be evaluated. Applications of the principle to measure the change of position of metal plate, to gage liquid level, and to estimate low velocity of a moving object are found in chapters III and IV. Signals of the measurement system to probe the phase are analyzed.

2.1 Interaction of electromagnetic wave with dielectric plate

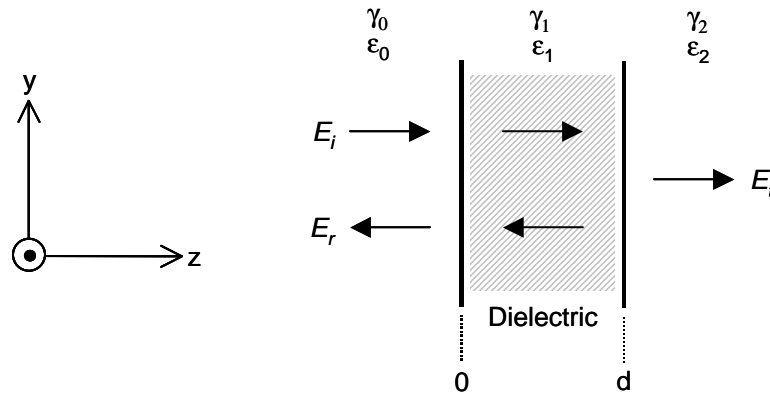


Fig. 2.1. Geometry involved in the analysis.

Figure 2.1 illustrates the geometry involved in the analysis of interferometry. It is assumed that the dielectric is located in the far field so that the incident electromagnetic wave is a plane wave. The electromagnetic wave normally incident on the dielectric and traveling in the z direction is expressed as

$$E_i(z, t) = E_0 \exp(j\omega t - \gamma z) \quad (2.1)$$

where γ is the propagation constant. The wave reflected E_r and transmitted E_t are determined by applying boundary conditions across the individual boundaries. The following expressions [7] are obtained from the boundary conditions:

$$\begin{aligned} E_0(1 + \Gamma_0) &= E_1(1 + \Gamma_1) \\ \frac{E_0}{Z_0}(1 - \Gamma_0) &= \frac{E_1}{Z_1}(1 - \Gamma_1) \\ E_1(e^{\gamma d} + \Gamma_1 e^{-\gamma d}) &= T_0 E_0 \\ \frac{E_1}{Z_1}(e^{\gamma d} - \Gamma_1 e^{-\gamma d}) &= T_0 \frac{E_0}{Z_2} \end{aligned} \quad (2.2)$$

where Γ and T are reflection and transmission coefficients, respectively; the subscript number corresponds to each medium; Z denotes impedance; and d is the thickness of dielectric. Solving the equations in (2.2) for Γ_0 and T_0 respectively, we can calculate the components of reflected and transmitted wave [7]. The reflected wave is obtained by

$$E_r = \Gamma_0 E_0 \quad (2.3)$$

where

$$\Gamma_0 = \frac{\left(\frac{Z_2}{Z_o} - 1\right) \cosh(\gamma_1 d) - \left(\frac{Z_1}{Z_o} - \frac{Z_2}{Z_1}\right) \sinh(\gamma_1 d)}{\left(\frac{Z_2}{Z_o} + 1\right) \cosh(\gamma_1 d) - \left(\frac{Z_1}{Z_o} + \frac{Z_2}{Z_1}\right) \sinh(\gamma_1 d)}.$$

And the transmitted wave is expressed by

$$E_t = T_0 E_0 \quad (2.4)$$

where

$$T_0 = \left\{ \frac{1}{2} \left[\left(1 + \frac{Z_0}{Z_2} \right) \cosh(\gamma_1 d) - \left(\frac{Z_1}{Z_2} + \frac{Z_0}{Z_1} \right) \sinh(\gamma_1 d) \right] \right\}^{-1}.$$

It is the wave defined in (2.3) or (2.4) that constructs the measurement path wave in an interferometry.

2.2 Determination of relative dielectric constant and thickness

The relative permittivity or dielectric constant (ϵ_r) as well as relative permeability (μ_r) characterize the relationship between electromagnetic waves and material properties. For a lossy material, the relative dielectric constant can be expressed in the complex form of

$$\bar{\epsilon}_r = \frac{\bar{\epsilon}}{\epsilon_0} = \epsilon_r + j \frac{\sigma}{\omega \epsilon_0} \quad (2.5)$$

where ϵ_r is the relative dielectric constant, ϵ_0 is the dielectric constant of free space, σ is

the conductivity of the material, and ω is angular frequency of electromagnetic waves. In reality, it is common to introduce dielectric loss tangent $\tan \delta$ to represent the complex dielectric constant; that is,

$$\bar{\epsilon}_r = \epsilon_r (1 + j \tan \delta) \quad (2.6)$$

where the dielectric loss tangent is defined as the ratio of imaginary to real component of the complex dielectric constant. The relative dielectric constant of the material located in free space can be determined on the basis of phase or amplitude measurement of either reflected or transmitted waves. In the measurement using the reflection method, the dielectric is typically conductor-backed to increase reflected power. In this case, Z_2 is equal to zero. Then, we can simplify the reflection coefficient in (2.3) as [7]

$$\Gamma_0 = \frac{(\gamma_0 - \gamma_1) \exp(-\gamma_1 d) - (\gamma_0 + \gamma_1) \exp(\gamma_1 d)}{(\gamma_0 + \gamma_1) \exp(-\gamma_1 d) - (\gamma_0 - \gamma_1) \exp(\gamma_1 d)} \quad (2.7)$$

substituting impedance Z_l in terms of free space impedance Z_0 ; i.e.,

$$Z_l = \frac{Z_0}{\sqrt{\epsilon_{rl}}} = \frac{\gamma_0}{\gamma_1} Z_0. \quad (2.8)$$

Here we assume the dielectric has low loss. The phase of reflection coefficient depending on the relative dielectric constant and thickness is shown in Fig. 2.2, as an example, where ϵ_{rl} implies the relative dielectric constant of the dielectric to be evaluated. In the measurement using the transmission method, the dielectric is located in free space between two antennas. Therefore, $Z_2 = Z_0$ and $\gamma_2 = \gamma_0$ are satisfied. Then the transmission coefficient in (2.4) can be transformed into [7]

$$T_0 = \frac{4\gamma_1\gamma_0}{(\gamma_0 + \gamma_1)^2 \exp(-\gamma_1 d) - (\gamma_0 - \gamma_1)^2 \exp(\gamma_1 d)} \quad (2.9)$$

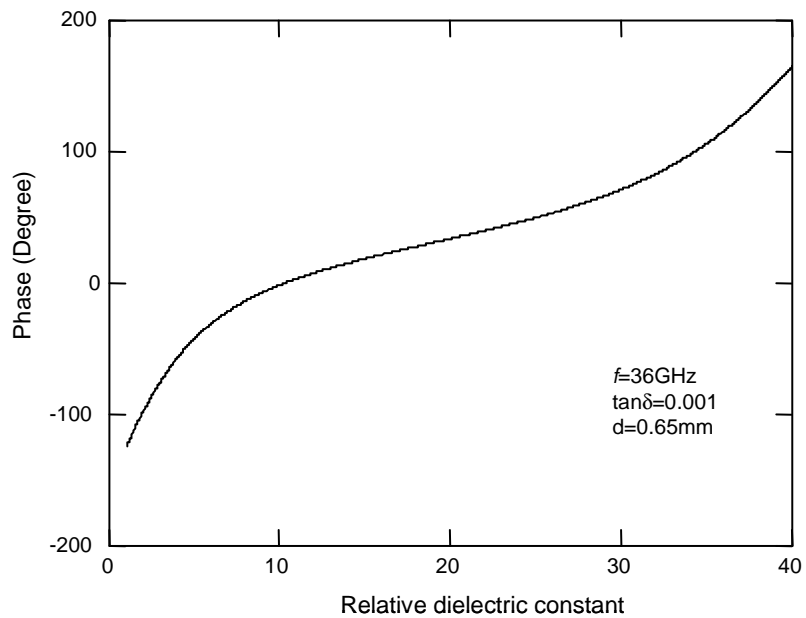
Figure 2.3 shows the phase variation of transmission coefficient of (2.9) corresponding to the change of relative dielectric constant and thickness. Note that the reflected and transmitted wave depicted in (2.3) and (2.4), respectively, represent the measurement path wave in the microwave interferometer.

2.3 Signal analysis of microwave interferometer

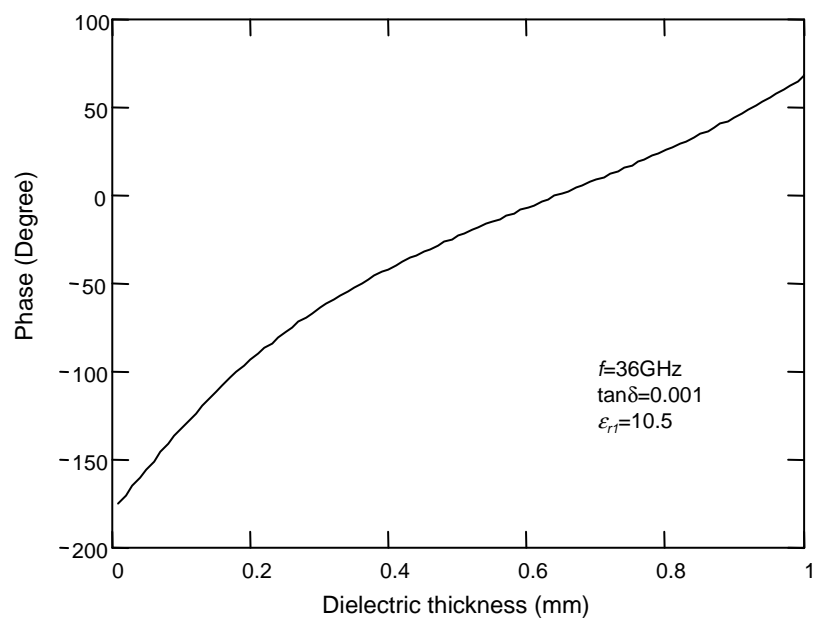
The principle of a microwave interferometer is based on the detection of phase difference between the reference path wave and the measurement path wave that is derived in equation (2.3) and (2.4) for the two different measurement approaches; reflection and transmission method. In the previous section, it was seen that the phase of reflection and transmission coefficient could be related to the relative dielectric constant and thickness. This section is devoted to signal analysis of a microwave interferometer to detect the phase. With the help of a schematic diagram of a typical microwave interferometer shown in Fig. 1.2 and 1.3, the system analysis is discussed as follows.

The power of the microwave signal source in the schematic, constituting reference path signal $v_{ref}(t)$ and measurement path signal $v_{mea}(t)$, is divided into two paths by a power divider. The $v_{ref}(t)$ is usually used as a local oscillator (LO) signal to pump the phase detecting processor, quadrature mixer. The $v_{mea}(t)$ is configured as one of the signals of (2.3) and (2.4) depending on the measurement method (reflection or transmission measurement). Those signals can be simply represented by sinusoidal signals as followings:

$$\begin{aligned} v_{ref}(t) &= A_r \cos(\omega t + \phi_{i1} + \phi_n) \\ v_{mea}(t) &= A_m \cos[\omega t + \phi(t) + \phi_{i2} + \phi_n] \end{aligned} \quad (2.10)$$

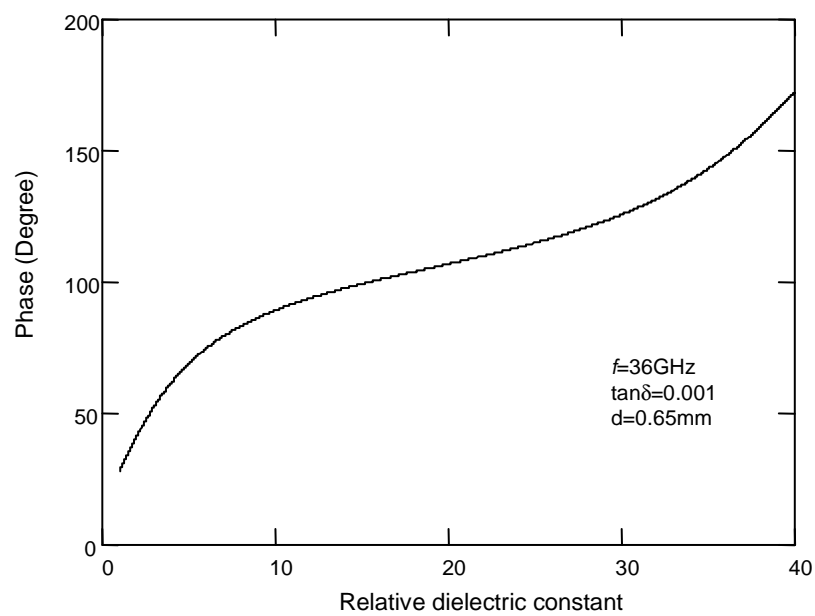


(a)

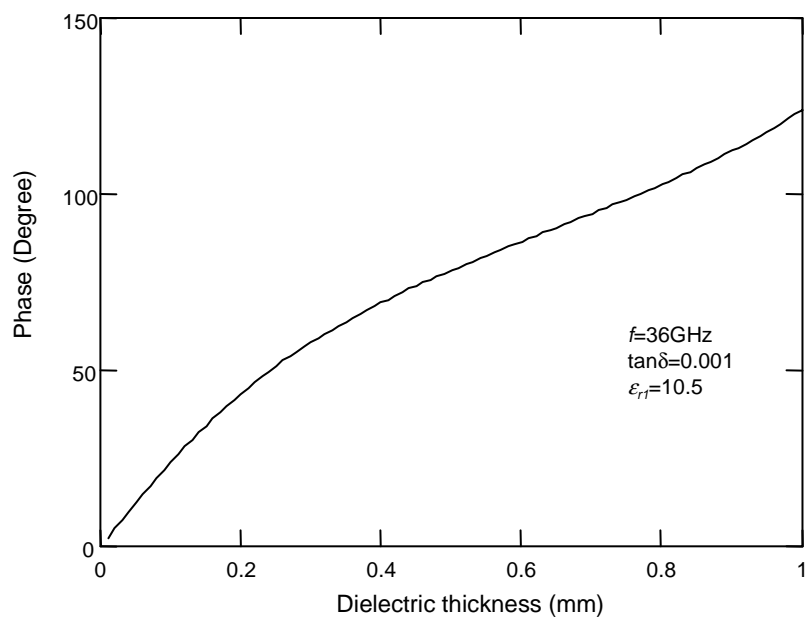


(b)

Fig. 2.2. Phase of reflection coefficient depending on (a) relative dielectric constant (b) dielectric thickness.



(a)



(b)

Fig. 2.3. Phase of transmission coefficient depending on (a) relative dielectric constant (b) dielectric thickness.

where A_r and A_m are amplitudes of each path signal; ϕ_{i1} and ϕ_{i2} are initial phases that come from the difference of electrical length in each path; ϕ_n is the phase noise of microwave signal source, which will be discussed in chapter IV; and $\phi(t)$ is the phase difference between the reference path and measurement path signal excluding the initial phase and can be considered as the phase of reflection or transmission coefficient in (2.7) and (2.9) if the contribution from initial phases in (2.10) is eliminated. When we need to measure the phase of reflection or transmission coefficients, we can insert a phase shifter-either in the reference or measurement path-to nullify the initial phase of both reference and measurement signals so that phase difference in (2.10) reads only the phase of reflection or transmission coefficient. The measurement path signal is weak because its power is attenuated while it propagates through the free space and dielectric. Thus it is usually amplified before it interferes with the reference path signal in the phase detecting processor. In the microwave interferometer, the quadrature mixer is generally used as a phase detecting device. Interfering with the two different waves (or signals), which is performed in the quadrature mixer, can be considered mathematically as a multiplication of these two signals. The measurement path signal, coherently interfered with the reference path signal and low pass filtered in the quadrature mixer, produces the following output signals in quadrature form:

$$\begin{aligned} v_I(t) &= A_I \cos[\phi(t) + \phi_{i1} + \phi_n] \\ v_Q(t) &= A_Q \sin[\phi(t) + \phi_{i2} + \phi_n] \end{aligned} \quad (2.11)$$

where subscript I and Q represent in-phase and quadrature, respectively, and A_I and A_Q are the amplitude of each quadrature signal. By applying inverse trigonometry, we can determine the phase $\phi(t)$, which is the ultimate goal of interferometry. It is important to notice that the actual response of the quadrature mixer does not exactly follow the form of (2.11) but responds nonlinearly due to its circuit imperfection, which is analyzed in the following chapter. The signals including nonlinearity of quadrature mixer can be described as

$$\begin{aligned} v_I(t) &= (A + \Delta A) \cdot \cos \phi(t) + V_{OSI} \\ v_Q(t) &= A \cdot \sin[\phi(t) + \Delta \phi] + V_{OSQ} \end{aligned} \quad (2.12)$$

where V_{OSI} and V_{OSQ} are DC offsets of the I and Q signals, respectively; and ΔA and $\Delta \phi$ represent the amplitude and phase imbalance between the I and Q channels, respectively; for convenience, initial phase terms and phase noise contribution are ignored here.

From the viewpoint of system, the function of the quadrature mixer in a microwave interferometer is fundamentally homodyne (or direct) down conversion of the measurement path signal. In addition to the imbalance issues described in (2.12), it is well known that 1/f noise contribution is a critical problem in the direct down conversion. The best strategy to overcome the problem is to slightly shift the frequency of either reference path or measurement path signal so that the frequency of the mixer's output signal is located far away from the 1/f noise spectrum. The schematic to implement this approach is shown in Fig. 1.4. The two input signals of the phase comparator in Fig. 1.4 are processed independently by two internal quadrature mixers to detect the phase difference between the two signals. Ignoring the initial phase and phase noise effect, we can express the output signals of the quadrature mixer, which is implemented by quadrature sampling digital signal processing technique in our system, as

$$\begin{aligned} v_I(nT) &= A \cdot \cos \phi(nT) \\ v_Q(nT) &= A \cdot \sin \phi(nT) \end{aligned} \quad (2.13)$$

where T is the sampling time of the digital quadrature mixer. The interferometer employing this approach is covered in chapter IV.

CHAPTER III

HOMODYNE INTERFEROMETRIC SENSOR*

Homodyne configuration has been the stereo type of the interferometer because of its simplicity. Most radio interferometry, especially for measurement purposes in laboratory, has been developed with this structure. Microwave interferometry has been used for various applications in instrumentation such as non-destructive characterization of material [7] and plasma diagnostics [8]. Interferometry is an ideal means for displacement measurement due to its high measurement accuracy and fast operation. Particularly, it has high resolution due to the fact that the displacement is resolved within a fraction of a wavelength of the operating frequency. Previous works based on optical interferometers have been reported for displacement measurements with resolution ranging from micrometer to sub-nanometer [9]-[11]. Fast and accurate displacement measurement is needed in various engineering applications such as high-speed metrology, position sensing, and liquid-level gauging.

This chapter presents the development of a new displacement-measurement interferometric sensor with sub-millimeter resolution. The system operates at 37.6 GHz and is completely fabricated using microwave and millimeter-wave integrated circuits – both hybrid (MIC) and monolithic (MMIC). It has been used to measure accurately the displacement of metal plate location and water level.

The non-linear phase response of the quadrature mixer, which is a critical problem in radio interferometry, is discussed along with a common I/Q error correction algorithm. The measurement error contributed to the quadrature mixer is estimated by a worst-case error analysis approach.

* © 2003 IEEE. Parts of this chapter are reprinted, with permission, from Seoktae Kim and Cam Nguyen, “A displacement measurement technique using millimeter-wave interferometry,” *IEEE Transactions on Microwave Theory and Techniques*, vol. 51, pp.1724-1728, June 2003

3.1 System configuration and principle

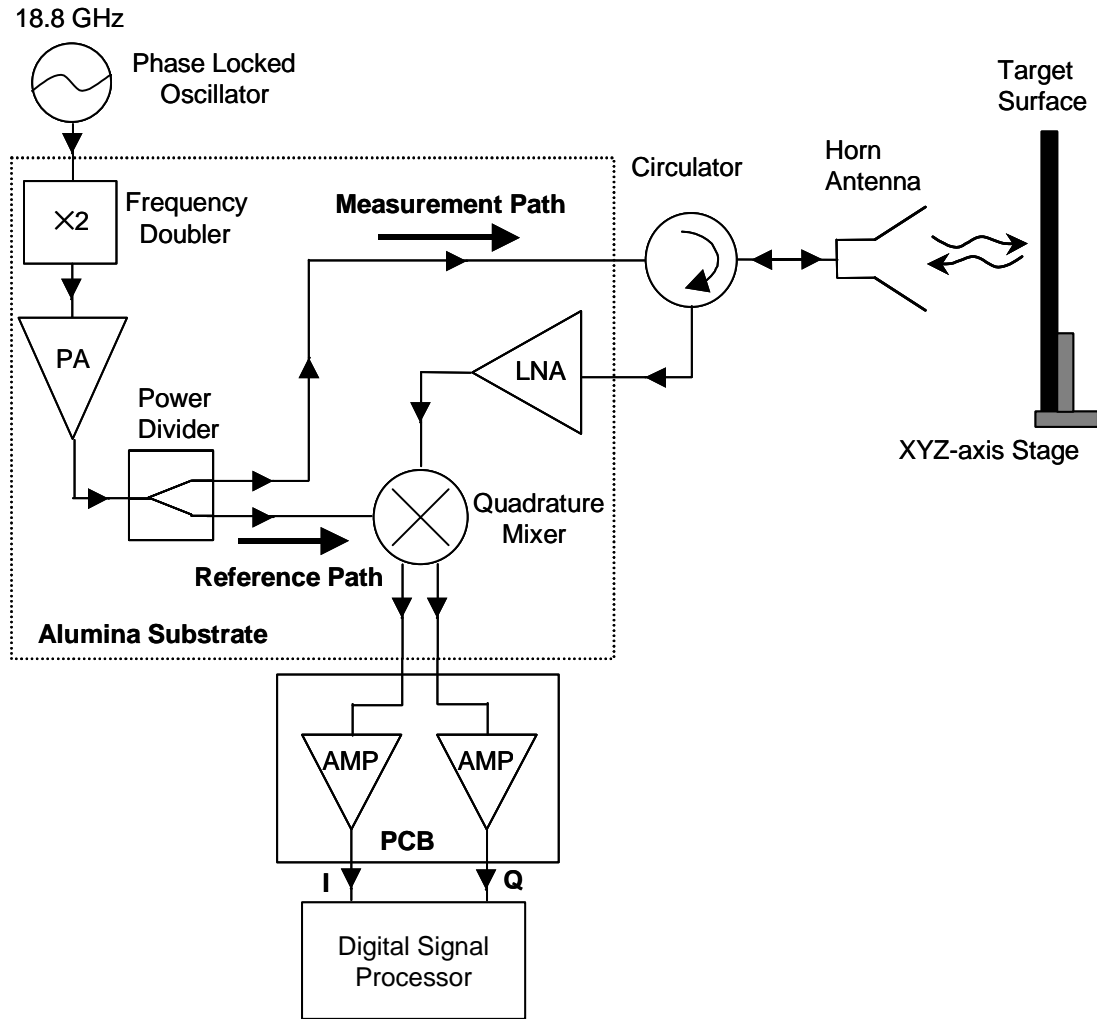


Fig. 3.1. Overall system configuration.

Fig. 3.1 shows the overall system block diagram. The sensor transmits a millimeter-wave signal to illuminate a target via the antenna. As depicted in section 2.3, the return signal from the target is captured by the sensor via the antenna and converted into a base-band signal, which is then processed to determine the displacement of the target location.

Displacement measurement using the interferometry technique is basically a coherent phase-detection process using a phase detecting processor, which is the quadrature mixer in the system. The phase difference between the reference and measurement paths, produced by a displacement of the target location, is determined from the in-phase (I) and quadrature (Q) output signals of the quadrature mixer. These signals are described as

$$\begin{aligned} v_I(t) &= A_I \sin \phi(t) \\ v_Q(t) &= A_Q \cos \phi(t) \end{aligned} \quad (3.1)$$

where A_I and A_Q are the maximum amplitudes of I and Q signals, respectively. $\phi(t)$ represents the phase difference and can be determined, for an ideal quadrature mixer, as

$$\phi(t) = \tan^{-1} \left(\frac{v_I(t)}{v_Q(t)} \frac{A_Q}{A_I} \right) \quad (3.2)$$

Practical quadrature mixers, however, have a nonlinear phase response due to their phase and amplitude imbalances as well as DC offset. A more realistic form of the phase including the nonlinearity effect can be expressed as

$$\phi(t) = \tan^{-1} \left(\frac{1}{\cos \Delta\phi} \frac{A}{(A + \Delta A)} \frac{v_I(t) - V_{OSI}}{v_Q(t) - V_{OSQ}} - \tan \Delta\phi \right) \quad (3.3)$$

by solving equation (2.12) for $\phi(t)$. The detected phase is generated by the time delay, τ , due to round-trip traveling of the electromagnetic wave for the distance between antenna aperture and target. Therefore it has a relationship with range, r , as following:

$$\phi(\tau) = 2\pi f_0 \tau = \frac{4\pi f_0 r}{c} \quad (3.4)$$

where f_0 and c are the operating frequency and speed in free space of the electromagnetic wave. From equation (3.4), the range as a function of time variable can be defined by

$$r(t) = \frac{\phi(t)}{4\pi} \lambda_0 \quad (3.5)$$

where λ_0 , defined by c/f_0 , is the operating wavelength in air, and normal incidence of the wave is assumed. Note that the detected phase corresponds to a round-trip travel of the received signal. Range variation is produced by changes in target location and can be expressed in the time domain as

$$\Delta r(nT) = r[nT] - r[(n-1)T] \quad n = 1, 2, 3, \dots \quad (3.6)$$

where T is the sampling interval. The displacement for the entire target measurement sequence can be described as a summation of consecutive range variations:

$$d(nT) = \sum_{n=1}^k \Delta r(nT) \quad n = 1, 2, 3, \dots, k \quad (3.7)$$

These range variations can be measured from the data acquisition and processing of the quadrature mixer's output signals, from which an actual displacement can then be constructed. In this displacement construction process, the range ambiguity problem arises due to the 2π -phase discontinuity of the phase detecting processor, which is typically expected in the interferometry technique. This problem is overcome by employing the phase unwrapping signal-processing technique described in [12]-[14]. Measured data produced by the interferometer are wrapped into the range $(-\pi, \pi]$, and the phase unwrapping algorithm is used to reconstruct the wrapped phase beyond the range of $(-\pi, \pi]$ so as to obtain a continuous phase without the 2π radian ambiguities.

3.2 Phase unwrapping signal processing

The phase unwrapping is an essential signal processing technique in interferometric radar. It is applied mainly for synthetic aperture radar (SAR) interferometry, magnetic resonance imaging (MRI) and astronomical imaging. The interferometric signals generated by the phase detecting device, which is the quadrature mixer in the developed system, are wrapped into the range $(-\pi, \pi]$. The goal of phase unwrapping signal processing is to reconstruct the wrapped phase beyond the range of $(-\pi, \pi]$. Mathematically, the phase unwrapping operation is described by the following equation in discrete time domain

$$\Phi(n) = \varphi(n) + 2\pi k(n) \quad (3.8)$$

where $\varphi(n)$ is an unwrapped phase which is the quantity to be detected, and $k(n)$ is an integer function that enforces $\varphi(n)$ wrapped.

Several digital techniques [12]-[14] have been proposed to develop the phase unwrapping algorithms. Itoh developed a brief and suggestive technique for a one-dimensional case [12]. For a brief discussion of Itoh's method, let us first introduce two operators W and Δ . The operator W wraps the phase into the range $(-\pi, \pi]$

$$W\{\varphi(n)\} = \Phi(n) + 2\pi k(n), \quad n = 0, 1, \dots, N-1 \quad (3.9)$$

where $k(n)$ is an integer array selected to satisfy $-\pi < \Phi(n) \leq \pi$.

The difference operator Δ is defined as

$$\begin{aligned} \Delta\{\varphi(n)\} &= \varphi(n+1) - \varphi(n) \\ \Delta\{k(n)\} &= k(n+1) - k(n) \end{aligned} \quad n = 0, 1, \dots, N-1. \quad (3.10)$$

From the difference of wrapped phase sequences using equations (3.9) and (3.10), we can get the following equation:

$$\Delta\{W\{\varphi(n)\}\} = \Delta\{\varphi(n)\} + 2\pi\Delta\{k_1(n)\}. \quad (3.11)$$

Applying the wrapping operation again to the above yields [12]

$$W\{\Delta\{W\{\varphi(n)\}\}\} = \Delta\{\varphi(n)\} + 2\pi[\Delta\{k_1(n)\} + k_2(n)] \quad (3.12)$$

where $k_1(n)$ and $k_2(n)$ distinguish the integer arrays produced by the two consecutive wrapping operations. Equation (3.12) implies $\Delta\{k_1(n)\} + k_2(n)$ should be zero to satisfy the requirement of $-\pi < \Delta\{\varphi(n)\} \leq \pi$. Thus it is reduced to

$$W\{\Delta\{\varphi(n)\}\} = \Delta\{\varphi(n)\} \quad (3.13)$$

Finally, the integration form of equation (3.13) shows that

$$\varphi(m) = \varphi(0) + \sum_{n=0}^{m-1} W\{\Delta\{W\{\varphi(n)\}\}\}. \quad (3.14)$$

Equation (3.14) implies that the actual phase sequences can be unwrapped by iterative integration operation of the wrapped difference of wrapped phases.

Fig 3.2 illustrates an example of phase unwrapping for a one-dimensional case. The sinusoidal phase sequence of equation (3.15) with maximum phase variation of 5π is perfectly reconstructed by phase unwrapping operation

$$\varphi(t) = 5\pi \sin(2\pi ft). \quad (3.15)$$

The f in the parenthesis implies a periodicity of the phase signal, such as vibration which may come from a periodic displacement of the target. The solid line in Fig. 3.2 represents the original phase function of (3.15). The reconstructed and wrapped phase sequences are designated by (O) and (\times), respectively. Typically, the wrapped phase is the form obtained by the phase detecting processor in most interferometric sensor. As shown, the unwrapped phase sequences are exactly reconstructed from the wrapped by applying phase unwrapping signal processing.

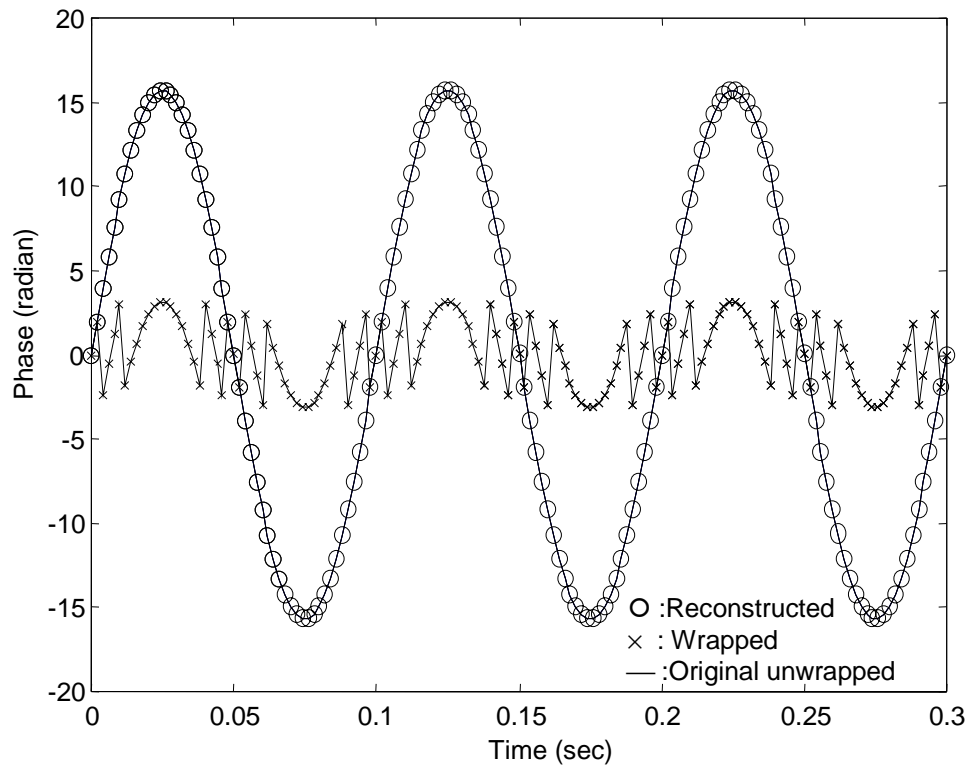


Fig. 3.2. Original unwrapped, wrapped and reconstructed phase sequences.

3.3 System fabrication

The millimeter-wave interferometric sensor has been fabricated using MICs and MMICs. All components inside the dotted lines shown in Fig. 3.1 are integrated on a 10-mil thick alumina substrate using surface-mount technology. The Wilkinson power divider, the counterpart of a beam splitter in optical interferometry, was analyzed by field simulation using a commercial field simulator, IE3D [15], and implemented on the top of alumina employing thin film technology, to direct the millimeter wave signal into the reference and measurement paths. The return loss and isolation were optimized to achieve better than 15 dB and 30 dB, respectively, at the frequency ranging from 36 to 38GHz. The resistor in the power divider was implemented with Ta₂N thin film, and adjusted accurately to obtain its final value, 100 Ω , using laser trimming. Fig. 3.3 shows the layout of the millimeter wave circuit part in detail.

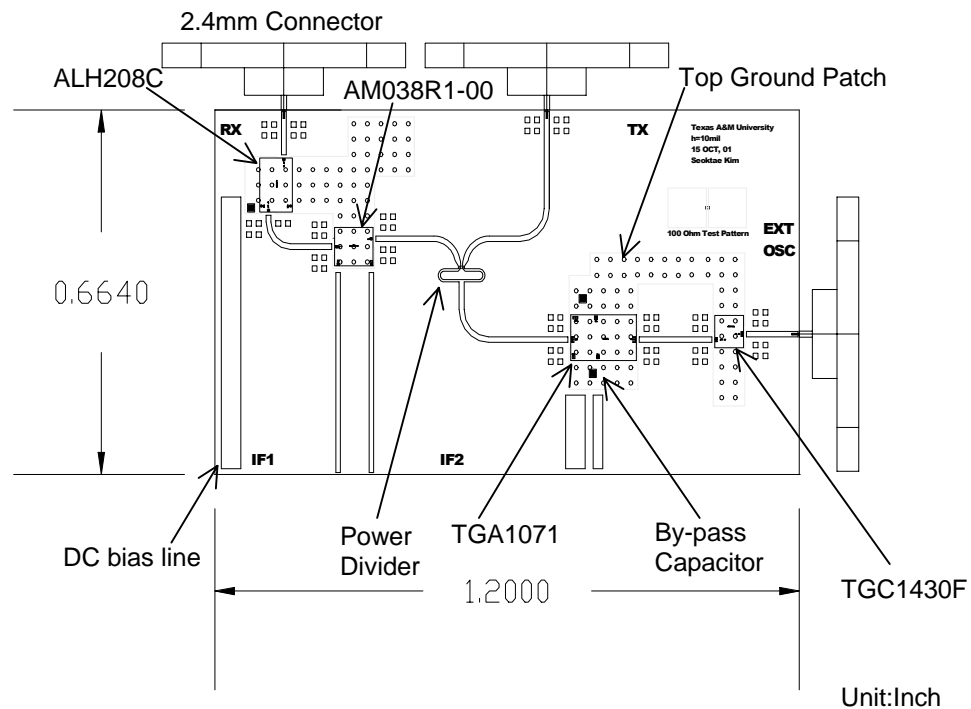


Fig. 3.3. Millimeter wave circuit layout in detail.

Commercially available Ka-band (26.5-40GHz) MMICs were used for the quadrature mixer (Alpha industries, AM038R1-00), low noise amplifier (TRW, ALH208C), power amplifier (TriQuint, TGA1071-EPU) and frequency doubler (TriQuint, TGC1430F-EPU); they are surface-mounted on metallic patches, which are gold plated and connected to the alumina's ground plane by 0.2-mm-diameter vias. A Printed Circuit Board (PCB) is used to mount a high-precision operational amplifier, which constitutes a 100-Hz pass-band active low pass filter. The filter provides gain for the output signals of the quadrature mixer and limits the signal bandwidth to reduce the noise-floor level. 3-by-0.5-mil gold ribbons are used to connect the 10-mil-wide alumina transmission lines to the signal pads on the MMICs. Fig. 3.4 is a photograph of the fabricated system.

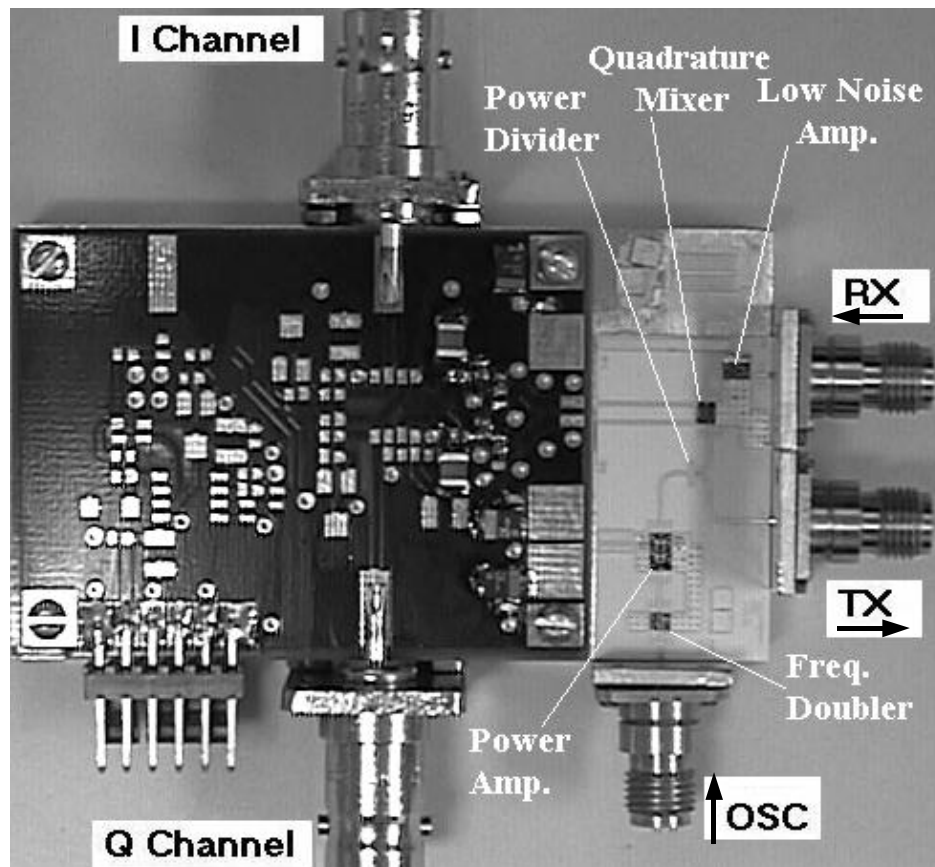


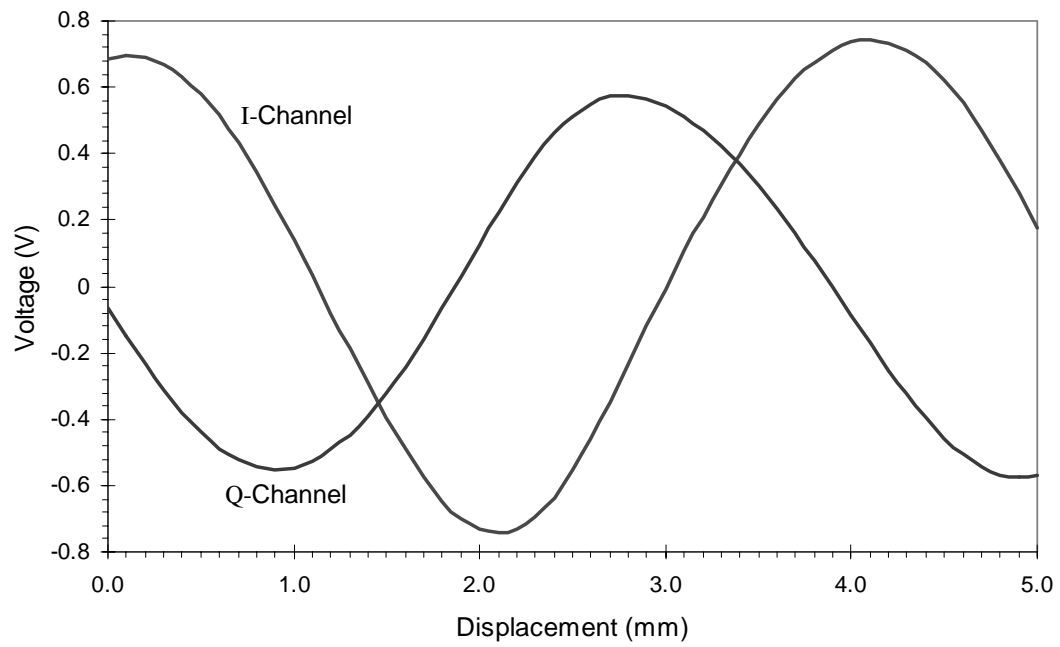
Fig. 3.4. Photograph of the fabricated system.

3.4 Displacement measurement and liquid-level gauging

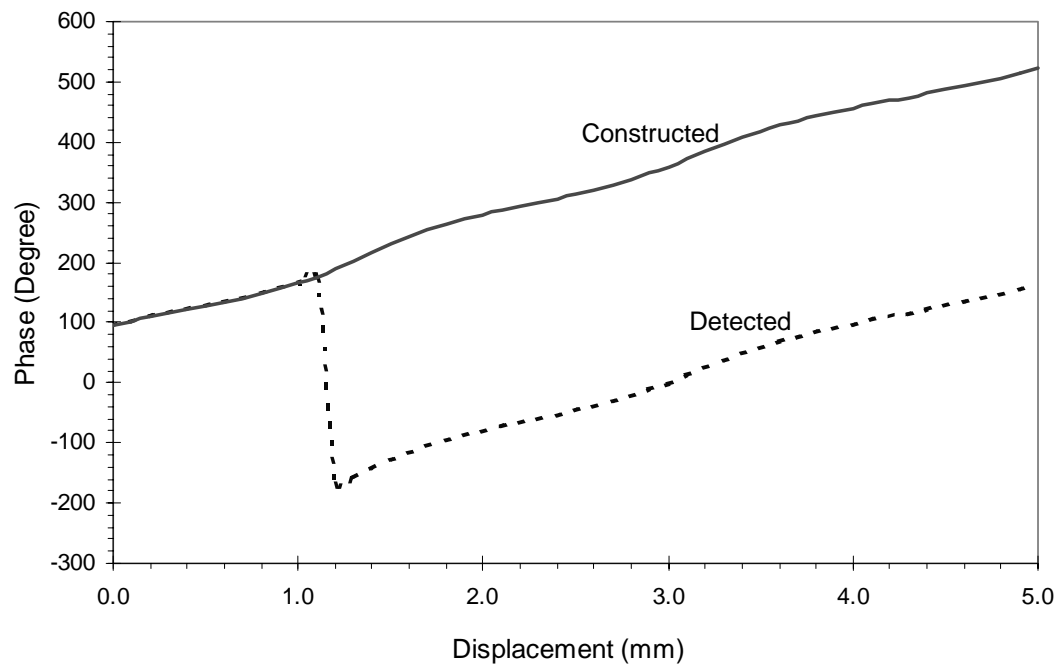
The measurement was performed using two laboratory test samples. An 18.8-GHz phase-locked source and a Ka-band standard horn antenna were used in the tests. The first sample is a metal plate mounted on a XYZ-axis stage. The XYZ-axis stage has a fine variation precision of 0.01 mm, a high accuracy of 0.002032 mm/25.4 mm and a good repeatability of 0.00127 mm. The metal plate was located 30-cm away from the antenna aperture, and the displacement measurement was made as the plate was moved every 0.1 mm. Signals from the quadrature mixer were captured by the data acquisition hardware (National Instruments, PCI-6111E) with the sample speed of 1kS/s and sample number of 1000. Then the entire set of samples is averaged to cancel out the noise components, which are composed of phase noise of the microwave signal source and white noise generated by circuits in the system. Fig. 3.5(a) shows the measured signal voltages, excluding DC-offset voltage, needed for the phase unwrapping. Fig. 3.5(b) displays the phase detected and constructed by the phase unwrapping technique. The phase detected was determined from

$$\phi(t) = \tan^{-1} \left(\frac{v_I(t) - V_{OSI}}{v_Q(t) - V_{OSQ}} \right) \quad (3.16)$$

which contains the errors resulting from the amplitude and phase imbalances of the quadrature mixer. As can be seen in Fig. 3.5(b), the reconstructed phase varies from 95 to 523 degrees for a displacement of 5 mm. This range of phase variation is sufficient to validate the phase unwrapping signal processing for phase reconstruction without the 360-degree ambiguities. For displacements corresponding to multiple times of 360 degrees, repetition of the phase unwrapping process is needed to construct the phase. The final displacement result is shown in Fig. 3.6 together with the measurement error.



(a)



(b)

Fig. 3.5. Measured signal voltage (a) and detected and constructed phase (b).

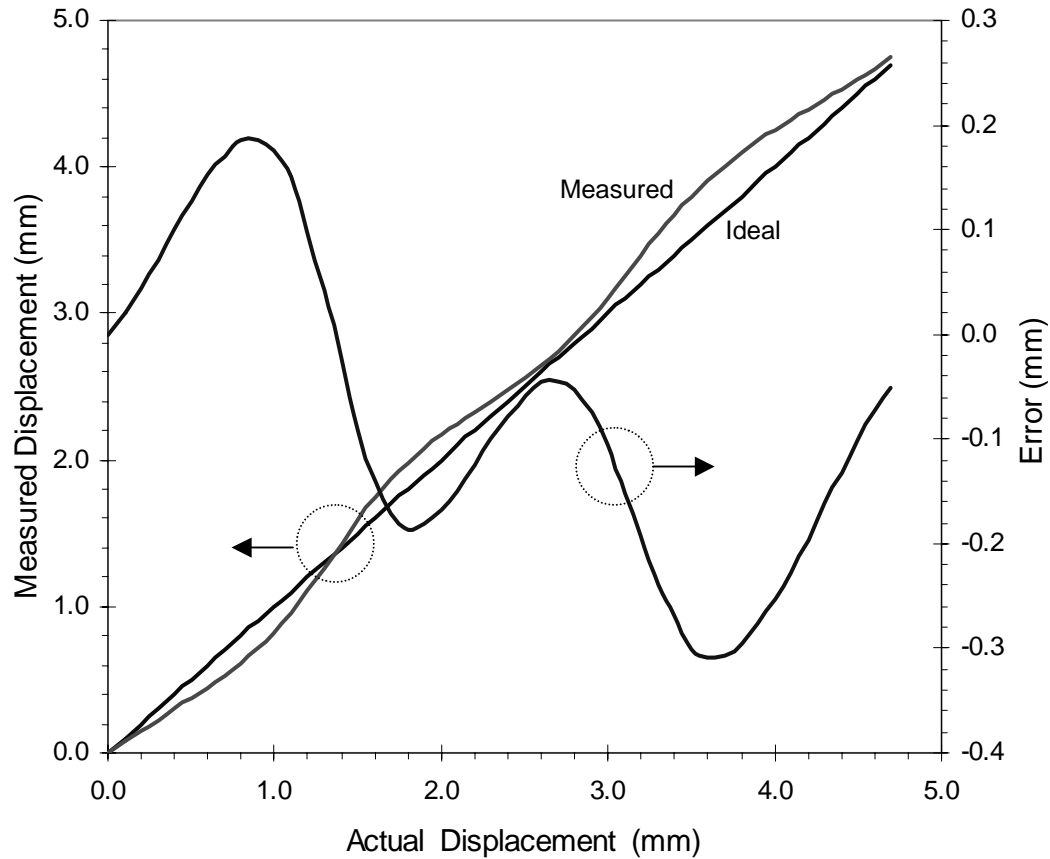


Fig. 3.6. Measured displacement for a metal plate.

The second sample, as shown in Fig. 3.7(a), is water stored in a reservoir, which is mounted on a XYZ-axis stage. It is used to demonstrate a possible application of liquid-level gauging. The water level was located at a distance of 15 cm from the horn antenna and the measurement was made as the distance was varied. Fig. 3.7(b) shows the measured displacement and corresponding error. In both measurements, the sensor achieves a measured resolution of only 0.05 mm and a maximum error of 0.3 mm at each displacement. The resolution was determined through the measurement of the minimum detectable voltage (or phase) as the displacement was varied.

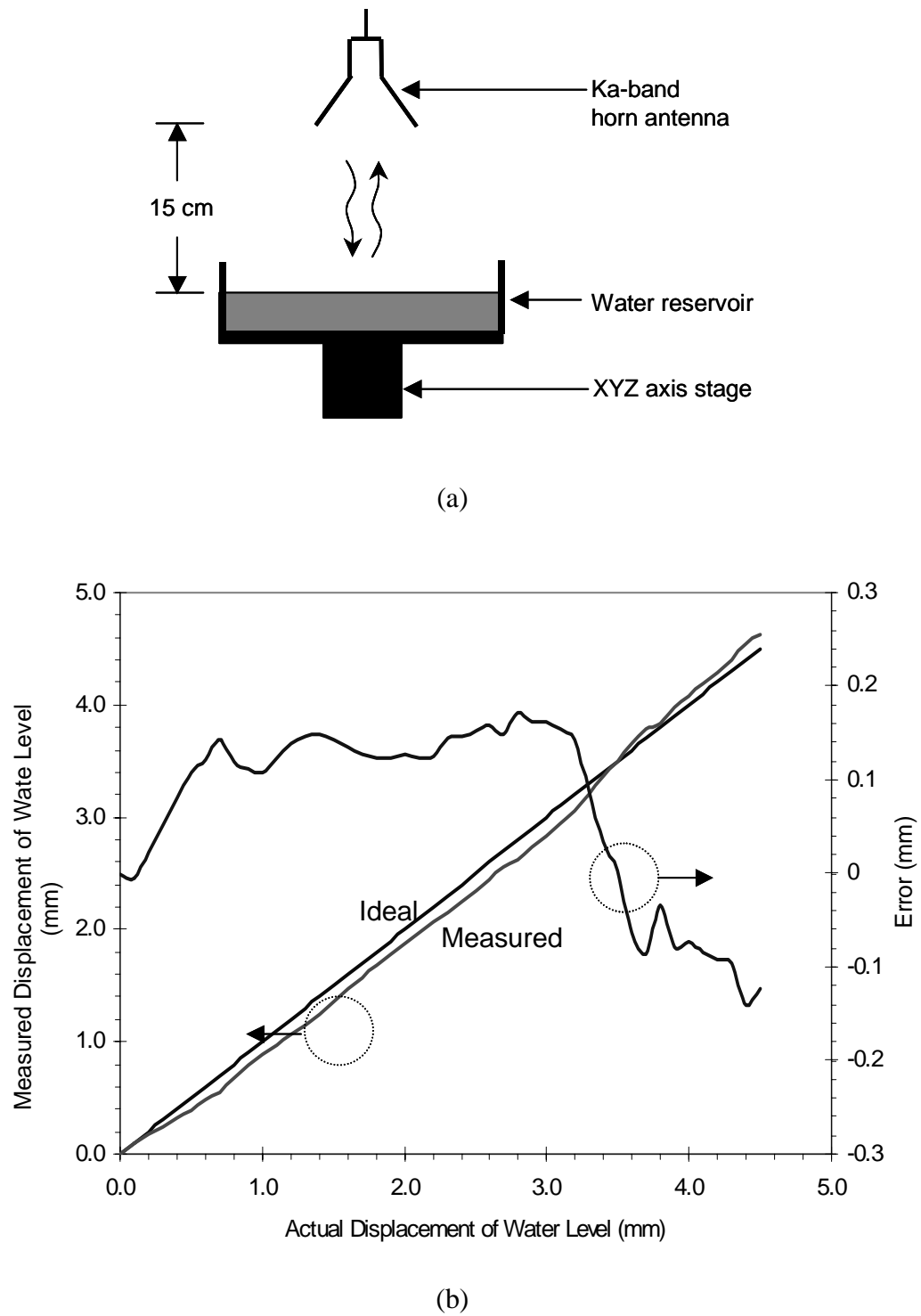


Fig. 3.7. Measurement set-up for water level gauging (a) and test results (b).

3.5 Error analysis contributed by quadrature mixer

3.5.1 Quadrature mixer transfer function

A quadrature mixer is the most common component used to detect phase in a microwave interferometer with a homodyne structure. Fig. 3.8 shows a typical functional block diagram of a quadrature mixer. It consists of basically two identically balanced mixers sharing a common in-phase RF input signal and a quadrature phase LO signal to pump the mixers. LO signal is fed into each mixer, split by 90 degrees hybrid. The conventional problem of a quadrature mixer, as a phase detecting processor, is that it is difficult to achieve good balance for the I and Q paths in terms of amplitude and phase, due to the imperfection of circuit components. This problem is usually called I/Q error, resulting in limitation in accuracy of interferometric measurement. As the operating frequency is increased, the problem becomes severe and hard to control.

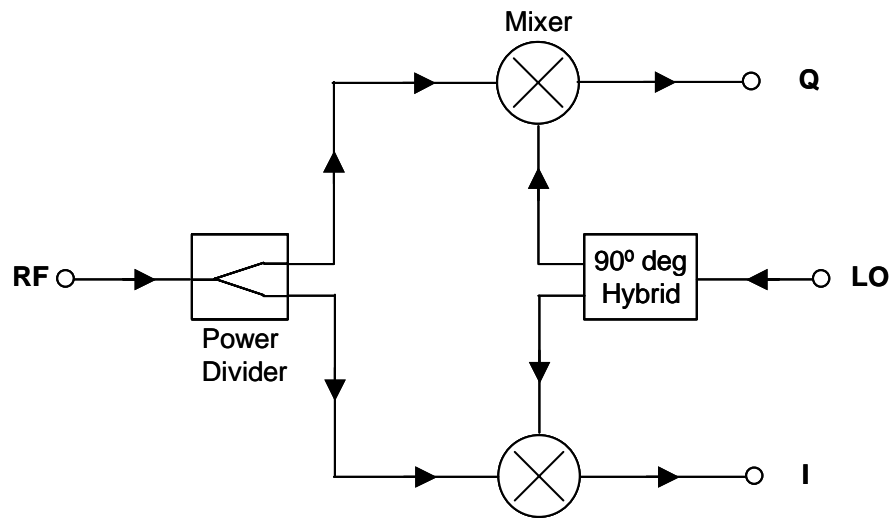


Fig. 3.8. Functional block diagram of quadrature mixer.

Equation (3.17) describes mathematically the ideal response of the quadrature mixer from the I and Q ports, assuming that the frequency of LO and RF signal is slightly offset by f_{IF} , i.e., $f_{RF} - f_{LO} = f_{IF}$

$$\begin{aligned} v_I(t) &= A \cdot \cos(2\pi f_{IF} t + \phi) \\ v_Q(t) &= A \cdot \sin(2\pi f_{IF} t + \phi) \end{aligned} \quad (3.17)$$

where ϕ is the phase information one wants to detect. Real response, however, is affected by the mixer's imperfection of amplitude and phase imbalance, causing I/Q error. The time response of the real quadrature mixer can be expressed as

$$\begin{aligned} v_I(t) &= (A \cdot \Delta A) \cos(2\pi f_{IF} t + \phi + \Delta\phi) + V_{OSI} \\ v_Q(t) &= A \sin(2\pi f_{IF} t + \phi) + V_{OSQ} \end{aligned} \quad (3.18)$$

where amplitude error is treated as the ratio of amplitudes for two signals. The actual phase detection process is performed with the detected signals of (3.18) excluding DC offset terms, because a band pass filter in the system easily filters out the DC offset. Therefore, the phase error produced by the non-ideal quadrature signals can be calculated by

$$\phi_e = \tan^{-1} \left[\frac{v_Q(t) - V_{OSQ}}{v_I(t) - V_{OSI}} \right] - \phi. \quad (3.19)$$

As an example, Fig 3.9 shows a non-linear phase response, accompanied by phase error corresponding to an amplitude imbalance of 2dB, phase imbalance of 10 degrees, and DC offset of 100mV. As seen, the phase response is non-linear for the linear change of input phase, and shows undulating behavior, which implies deterioration of measurement accuracy.

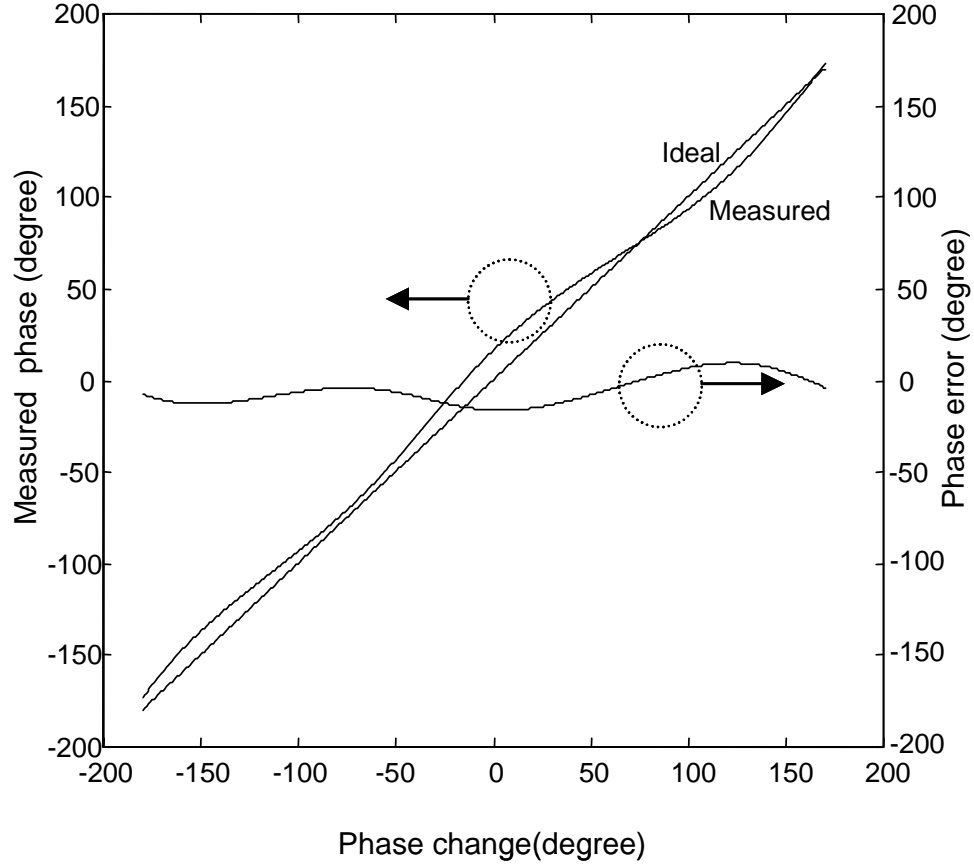


Fig. 3.9. Example of non-linear phase response of quadrature mixer.

In a homodyne system, the frequency of RF and LO signals is the same, so that the output of the quadrature mixer generates only DC terms. This makes the estimation of phase error difficult. It is a common approach to introduce a test signal, which is produced by mixing the RF signal with the LO signal slightly different from RF in frequency so that the output of the mixer is AC of intermediate frequency, f_{IF} . Usually, f_{IF} is chosen low enough to be processed by digital signal processing. Based on the test signals, it is possible to estimate amplitude and phase imbalance as well as DC offset of the quadrature mixer in frequency domain using fourier transform, as explained in detail in the following section.

It is convenient to handle the pair of signals in (3.18) as a complex signal; that is,

$$v(t) = v_I(t) + jv_Q(t) . \quad (3.20)$$

Applying fourier transform on (3.20) produces an impulse (delta) function in frequency domain. For an ideal quadrature mixer, the impulse function appears only at the frequency of f_{IF} . But imbalances of the quadrature mixer cause image response at the negative (or image) frequency of f_{IF} .

Equation (3.21) computes fourier transform of complex output signals of a real quadrature mixer.

$$\begin{aligned} \mathcal{F}[v(t)] &= \mathcal{F}[v_I(t) + jv_Q(t)] \\ &= \mathcal{F}(0) \quad : \text{DC term} \\ &+ \frac{1}{2} A \cdot \exp(j\phi) [\Delta A \cos(\Delta\phi) + j\Delta A \sin(\Delta\phi) - 1] \delta(f + f_{IF}) \quad : \text{Image Signal} \\ &+ \frac{1}{2} A \cdot \exp(j\phi) [\Delta A \cos(\Delta\phi) + j\Delta A \sin(\Delta\phi) + 1] \delta(f - f_{IF}) \quad : \text{Primary Signal} \end{aligned} \quad (3.21)$$

which constitutes a DC term that comes from DC offset, upper (Primary) and lower side (Image) signals. The power ratio of lower to upper signal, Image-to-Signal Ratio (ISR) measures the amount of deviation of the real quadrature mixer's response compared to an ideal response, and defined by

$$ISR = \frac{[\Delta A \cos(\Delta\phi) - 1]^2 + [\Delta A \sin(\Delta\phi)]^2}{[\Delta A \cos(\Delta\phi) + 1]^2 + [\Delta A \sin(\Delta\phi)]^2} . \quad (3.22)$$

From equation (3.22), amplitude imbalance is derived by [16]

$$\Delta A = \frac{\cos(\Delta\phi)(1 + ISR) + \sqrt{[\cos(\Delta\phi)(1 + ISR)]^2 - (1 - ISR)^2}}{1 - ISR} . \quad (3.23)$$

It is relatively easier to measure ISR and ΔA using a spectrum analyzer than to measure $\Delta\phi$. From the measured ISR and amplitude imbalance, phase imbalance can be therefore deduced as [16]

$$\Delta\phi = \cos^{-1} \left[\frac{(\Delta A^2 + 1)(1 - ISR)}{2\Delta A(1 + ISR)} \right]. \quad (3.24)$$

Figure 3.10 illustrates the frequency response of a complex output signal of a quadrature mixer for both ideal and real cases. The image signal shown in the figure is generally called Hermitian image; it produces a false target and deteriorates resolution in radar used for most ranging applications. Also, in interferometry, it causes a non-linear phase response, as already shown in Fig. 3.9. It is thereby desirable to suppress or eliminate the image signal.

3.5.2 I/Q error correction algorithm

As discussed in the previous section, the image signal influences quadrature phase detection in interferometric radar. In most radar and communication applications, it is desirable to correct the I/Q error. In this section, the most common method to correct I/Q error is presented by means of correction coefficients derived from the test signal [17]. Starting with representation of the quadrature signal with I/Q errors, we can express the quadrature signals as

$$\begin{aligned} v_I(t) &= (A + \Delta A) \cdot \cos(2\pi f_{IF} t) \\ v_Q(t) &= A \cdot \sin(2\pi f_{IF} t + \Delta\phi) \end{aligned} \quad (3.25)$$

where DC offset is excluded because it is simply determined by the averaged DC level (or zero frequency component in Fourier transform) of each quadrature channel signal.

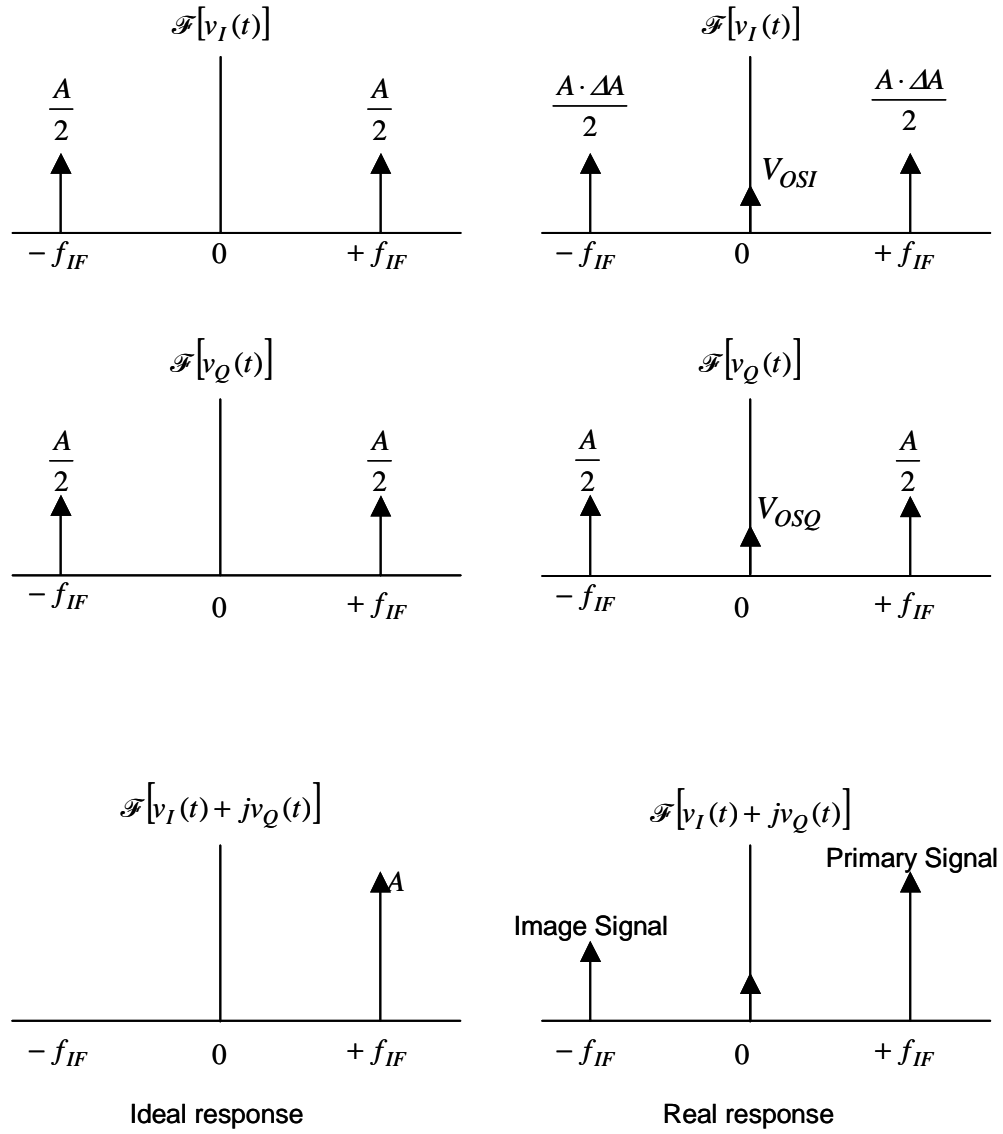


Fig. 3.10. Frequency response of ideal and real quadrature mixer.

The problem of I/Q error correction is analogous to Gram-Schmidt orthogonalization, designating quadrature signal with vector matrix notation, i.e.,

$$\begin{bmatrix} v'_I(t) \\ v'_Q(t) \end{bmatrix} = \begin{bmatrix} S & 0 \\ R & 1 \end{bmatrix} \begin{bmatrix} v_I(t) \\ v_Q(t) \end{bmatrix} \quad (3.26)$$

where S and R are rotating and scaling coefficients, respectively, to make the quadrature signals of (3.25) orthogonal; that is, exactly 90 degrees out of phase with equal amplitude. In [17], a digital signal processing technique is suggested to obtain estimates of the coefficient matrix using DFT (Discrete Fourier Transform). By definition, the DFT of complex quadrature signal $v(t)$ yields

$$\mathcal{F}\left(\frac{k}{NT}\right) = \frac{1}{N} \sum_{n=0}^{N-1} v(nT) \exp(-j \frac{2\pi kn}{N}) \quad k = 0, 1, 2, \dots, N-1 \quad (3.27)$$

where T is the sampling time, N is the number of samples, and $v(nT) = v_I(nT) + jv_Q(nT)$. And primary and image signal components, respectively, appear at $\mathcal{F}(1/NT)$ and $\mathcal{F}[(N-1)/NT]$ and are related to amplitude and phase imbalance by

$$\begin{aligned} \mathcal{F}\left(\frac{1}{NT}\right) &= \frac{A}{2} [(1 + \Delta A) + \cos(\Delta\phi) + j \sin(\Delta\phi)] \\ \mathcal{F}\left(\frac{N-1}{NT}\right) &= \frac{A}{2} [(1 + \Delta A) - \cos(\Delta\phi) + j \sin(\Delta\phi)], \end{aligned} \quad (3.28)$$

substituting (3.29) into (3.27), and solving for the DFT components at the frequencies of $1/NT$ and $(N-1)/NT$.

$$v(nT) = (A + \Delta A) \cdot \cos[2\pi f_{IF}(nT)] + jA \cdot \sin[2\pi f_{IF}(nT) + \Delta\phi]. \quad (3.29)$$

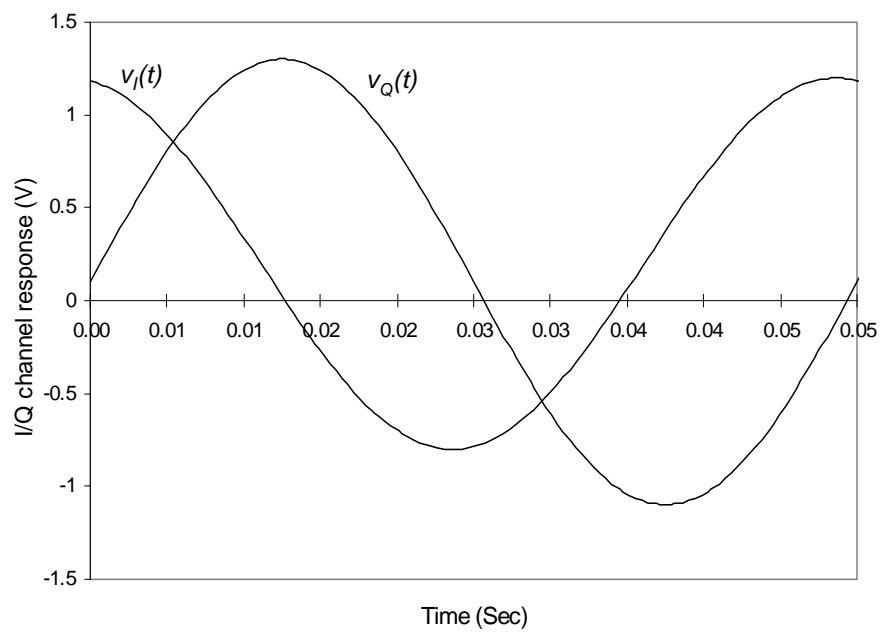
Then, the estimates of coefficients in (3.26) can be obtained by the components of DFT of (3.28) as [17]

$$\begin{aligned} \hat{S} &= -\text{Re} \left\{ \frac{2\mathcal{F} \left[\frac{(N-1)}{NT} \right]}{\mathcal{F}^* \left(\frac{1}{NT} \right) + \mathcal{F} \left[\frac{(N-1)}{NT} \right]} \right\} + 1 \\ \hat{R} &= -\text{Im} \left\{ \frac{2\mathcal{F} \left[\frac{(N-1)}{NT} \right]}{\mathcal{F}^* \left(\frac{1}{NT} \right) + \mathcal{F} \left[\frac{(N-1)}{NT} \right]} \right\} \end{aligned} \quad (3.30)$$

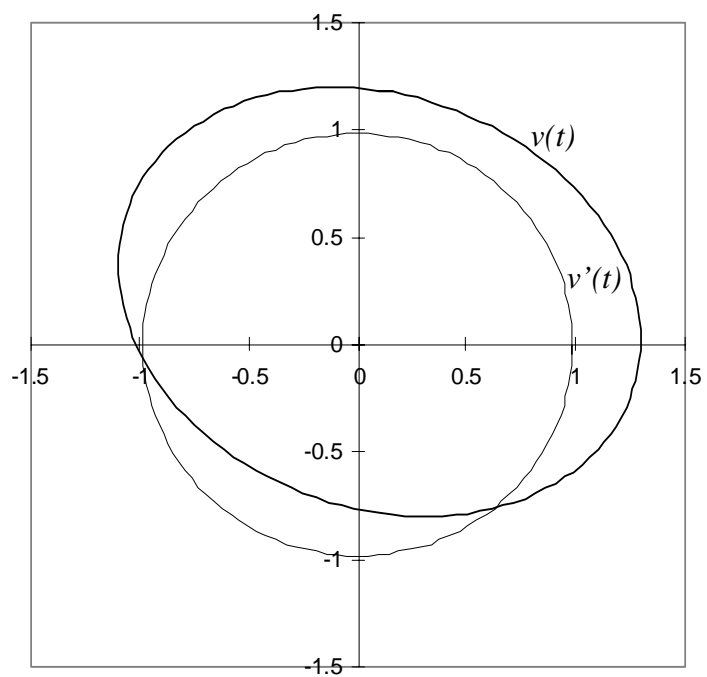
where \mathcal{F}^* means a conjugate of \mathcal{F} .

Fig. 3.11 shows an example of I/Q error correction by the coefficients obtained by DFT, where amplitude imbalance is 0.8dB, phase imbalance is 10 degrees, and DC offset voltage is 100mV for I channel and 200mV for Q channel, respectively.

Fig. 3.11(a) shows the quadrature signals corresponding to the imbalances mentioned above, and Fig. 3.11(b) demonstrates geometric interpretation of the correction process. If we plot the in-phase signal $v_I(nT)$ in X-axis, and the quadrature signal $v_Q(nT)$ in Y-axis, then they constitute an ellipse in the XY complex plane. From a geometric viewpoint, the procedure for correcting I/Q error can be interpreted as rotation and scaling of the ellipse in the XY complex plane, as shown in Fig 3.11 (b), so that it finally turns into a perfect circle centered at the origin. The coefficients of S and R defined in (3.26) can be geometrically interpreted as scaling and rotation coefficients to convert the right-most vector $v(t)$ in (3.26), which is neither orthogonal nor equal in amplitude, into the left-most vector $v'(t)$, which is orthogonal and equal in amplitude as in the centered circle in Fig. 3.11(b).



(a)



(b)

Fig. 3.11. I/Q error correction (a) I/Q channel response
(b) Geometric interpretation of I/Q error correction.

3.5.3 Worst-case error analysis

The measurement error employing the homodyne configuration is attributed mostly to the nonlinear response of the quadrature mixer. Several techniques have been proposed to correct the non-linearity of the quadrature mixer [17]-[18]. Possible sources of error also come from the measurement distance, the target's reflecting surface, or a combination of these. The instability of the frequency source should produce a negligible effect on the measurement due to the short time delay between the transmit and receive signals of the sensor. The sensor can also operate at larger ranges (e.g., 3 m) with proper transmitting power.

Measurement accuracy was estimated by an analysis of the maximum phase imbalance using the method proposed in [19]. In this method, the maximum phase error resulted from the image rejection level of the quadrature is calculated. From equation (3.22), the image-to-signal ratio (ISR) given as a function of the amplitude and phase imbalance can be reduced to

$$ISR = \frac{1 + \Delta V^2 - 2\Delta V \cos(\Delta\phi)}{1 + \Delta V^2 + 2\Delta V \cos(\Delta\phi)}. \quad (3.31)$$

Equation (3.31) can be approximated by an ellipse

$$\left(\frac{\Delta\phi}{X}\right)^2 + \left(\frac{\Delta V}{Y}\right)^2 = 1 \quad (3.32)$$

where

$$X = \cos^{-1}\left(\frac{1 - ISR}{1 + ISR}\right)$$

$$Y = \frac{1 + \sqrt{ISR}}{1 - \sqrt{ISR}}.$$

Fig. 3.12 shows constant ISR contours for several different ISR values of a quadrature mixer. As can be seen, the maximum phase imbalance occurs when the amplitude imbalance is 0 dB. Using an ISR of 18 dB from the employed quadrature mixer's data sheet [20], a maximum phase error was obtained as 14.4° , which corresponds to a maximum distance accuracy of 0.32-mm. The measured error of 0.3 mm shown in Fig. 3.6 and 3.7(b) falls within the maximum calculated error.

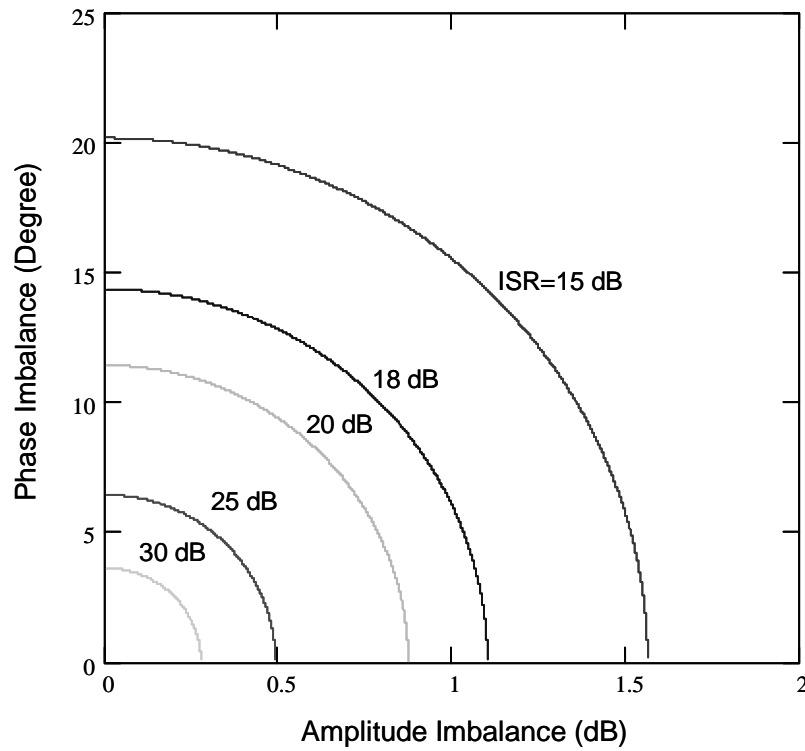


Fig. 3.12. Constant ISR contours.

3.6 Summary

A new millimeter-wave interferometric sensor with homodyne configuration, operating 37.6GHz, has been developed and demonstrated for accurate displacement sensing and liquid-level gauging. The sensor was integrated on alumina substrate and PCB, employing MMICs and MICs. It has been used to measure accurately the displacement of metal plate location and water level. From the experimental results, it has been found that sub-millimeter resolution in the order of 0.05 mm is feasible. A measurement accuracy of 0.3 mm was also determined and is within the maximum error calculated on the basis of worst-case error analysis for the I/Q error of the quadrature mixer. The developed sensor's performance is compared with those of some commercial liquid –level gauging sensors in Table 1, where the specifications of the commercial sensors are referred to in [21]. The measured results demonstrate the workability of the developed sensor and its potential as an effective tool for displacement measurement and liquid level-gauging.

Table 1. Comparison of the developed sensor's performance with those of commercial liquid-level gauging sensors.

	Developed Sensor	Saab (Tank Radar)	Pepperl + Fuchs
Sensing Technique	Interferometry (Single CW frequency)	FMCW	FMCW
Operating frequency	37.6GHz	X-Band Bandwidth: 1 GHz	24 GHz Bandwidth: 0.2 GHz
Accuracy	0.3mm	1cm	>20cm

CHAPTER IV

DOUBLE-CHANNEL HOMODYNE INTERFEROMETRIC SENSOR*

In this chapter, double-channel homodyne configuration is proposed to realize a millimeter wave interferometric sensor. The motive to adopt this configuration is to eliminate the non-linear phase response of the quadrature mixer, which critically limits the sensor's measurement accuracy. The prominent difference between the double-channel and homodyne configurations is that either measurement or reference path signal is modulated using a quadrature up-converter so that phase information can be detected at an intermediate frequency (IF), which is a frequency low enough to be handled with a digital signal processor. Then the phase is detected by the quadrature sampling digital signal processing technique. With this approach, it is possible to exclude the conventional imbalance problem of the quadrature mixer. Also the double-channel homodyne configuration provides additional advantage of estimating the phase noise effect of a millimeter wave frequency signal source using FFT algorithm, without the help of phase noise measurement equipment, due to the fact that the phase noise of a microwave source is down-converted and appears at IF.

A new multi-function millimeter wave sensor operating at 35.6 GHz has been developed and demonstrated for measurement of displacement and low velocity, based on the double-channel homodyne configuration shown in Fig. 1.4. The sensor was realized using MICs and MMICs. Measured displacement results show an unprecedented resolution of only 10 μm , which is approximately equivalent to $\lambda_0/840$ in terms of free-space wavelength λ_0 . A maximum error of only 27 μm was obtained after corrections using a polynomial curve fitting. Results indicate that multiple reflections dominate the displacement measurement error. For low-velocity measurement, experiments were performed in a laboratory for a moving target on a commercial

* © 2004 IEEE. Parts of this chapter are reprinted, with permission, from Seoktae Kim and Cam Nguyen, "On the development of a multi-function millimeter-wave sensor for displacement sensing and low-velocity measurement," *IEEE Transactions on Microwave Theory and Techniques*, vol. 52, pp. 2503-2512, Nov. 2004

conveyor. The sensor was able to measure speed as low as 27.7 mm/s, corresponding to 6.6 Hz in Doppler frequency, with an estimated velocity resolution of 2.7 mm/s. A digital quadrature mixer (DQM) was configured as a phase detecting processor, employing the quadrature sampling signal processing technique, to overcome the non-linear phase response problem of a conventional analog quadrature mixer. The DQM also enables low Doppler frequency to be measured with high resolution. The Doppler frequency was determined by applying linear regression on the phase sampled within only fractions of the period of the Doppler frequency. Short-term stability of a microwave signal source was also considered to predict its effect on measurement accuracy.

Microwave and millimeter-wave interferometry has been used widely for non-destructive material characterization [1],[22], plasma diagnostics [23], position sensing [24]-[25], velocity profile [26], cardio pulmonary [27], radio astronomy [28]-[29], topography [30], meteorology [31], precision noise measurement [32], displacement measurement [33], and low-velocimetry [34]. Interferometry is basically a phase-sensitive detection process, capable of resolving any measured physical quantity within a fraction of the operating wavelength. Interferometric sensors also have a relatively faster system response time than other sensors due to the fact that they are generally operated with single-frequency sources.

Microwave and millimeter-wave Doppler radar has drawn much attention in the automobile industry as a speed-detection sensor for intelligent cruise control, collision-avoidance, and antilock brake systems for vehicles [35]-[39]. An interferometer can be configured to perform the functions of both displacement sensing and velocity measurement, effectively working together as the interferometric displacement sensor and Doppler velocity sensor.

The previous chapter was devoted to the millimeter-wave interferometer with homodyne configuration as a displacement and liquid level-gauging sensor. This sensor has a resolution of 50 μm , which is equal to $\lambda_0/160$, with λ_0 being the free-space operating wavelength, and 0.3-mm maximum error. In this chapter, we present Doppler

velocimeter for low-velocity measurement as well as displacement sensing. In [40], a six-port wave-correlator was also developed to achieve the same purpose.

In this chapter, the development of a new multi-function millimeter wave sensor capable of measuring both displacement and velocity (particularly low velocity), based on phase detection, for potential industrial applications, is reported. The displacement sensing is achieved by configuring the sensor as an interferometric device. The velocity measurement is realized by detection and estimation of the Doppler frequency shift in base band, which is processed against a phase detected by the interferometric function of the sensor.

To achieve a resolution and maximum error of only 10 and 27 μm at 35.6 GHz, respectively, new system configuration and signal processing, along with a new error correction procedure, were developed and implemented for displacement sensing. To the best of our knowledge, the attained resolution, which is approximately equal to $\lambda_0/840$, is the best reported resolution in terms of wavelength.

In Doppler velocity measurement, a common method to estimate the Doppler frequency is the maximum likelihood estimate (MLE) obtained by determining the spectral peak centroid in a periodogram, which is implemented by combining Fast Fourier Transform (FFT) algorithm and numerical technique. In our approach, we employed a different approach using signal processing, based on quadrature phase detection in base band, to estimate the Doppler frequency by applying linear regression on the detected phase. This represents an effective way, particularly for estimating the low-frequency sinusoidal signal needed for low-velocity measurement, compared to the FFT-based MLE. The developed sensor for low-velocity measurement has potential to replace the laser Doppler velocimeter, especially in a humid and dusty environment, due to the fact that it is less sensitive than the laser-based velocity sensor to dust particles and water in the air.

4.1 System configuration and principle

The overall system configuration is shown in Fig. 4.1. The system is divided into three parts: a millimeter-wave subsystem for processing a millimeter-wave signal, an intermediate-signal subsystem for processing signals at intermediate frequencies, and a digital signal processor. The 17.8-GHz phase-locked oscillator, the Ka-band directional coupler, and the lens horn antenna are external components. The sensor transmits a millimeter-wave signal at 35.6 GHz toward a target. The directional coupler, providing good isolation between the transmit and receive ports, is used to direct the signal to the antenna. The signal reflected from the target is captured via the antenna, redirected by the coupler to the receiver circuitry, and up-converted by mixing with the RF signal produced by modulating the signal at the first intermediate frequency (IF), f_{IF1} , with the signal of the second intermediate frequency, f_{IF2} , in a direct quadrature up-converter. The up-converted signal is then passed through a coupled-line band pass filter to reject its image component. This signal is combined with part of the transmitted millimeter-wave signal to generate a down-converted RF signal, which is further down-converted by another down-converter in the intermediate-signal subsystem. f_{IF1} and f_{IF2} are chosen as 1.8 GHz and 50 KHz, respectively. Consequently, the final down-converted signal, $v_M(t)$, namely the measurement-channel signal, contains information on the phase or phase change over time generated by the target displacement or movement, respectively. It is finally amplified by a band-limited differential amplifier and transferred to the digital signal processor, through a twisted cable. The differential driving amplifier combined with the twisted cable provides good noise suppression as well as additional voltage gain. For the displacement measurement, the measured phase of $v_M(t)$ is compared with that of the reference-channel signal, $v_R(t)$, coming from the direct digital synthesizer (DDS). $v_R(t)$ also serves as an IF signal for the direct quadrature up-converter in the intermediate-signal subsystem. If the target is in motion, the frequency of $v_M(t)$ is shifted by the Doppler frequency. In velocity measurement, the phase change over time is detected in the signal processing, and the only measurement-channel signal is processed to extract the Doppler frequency shift. Instead of employing an analog

millimeter-wave quadrature mixer as in the previous work [33], a digital quadrature mixer was configured as a phase detecting processor based on quadrature sampling to detect the phase difference between the reference- and measurement-channel signals for displacement measurement and the phase change over time for Doppler velocimetry.

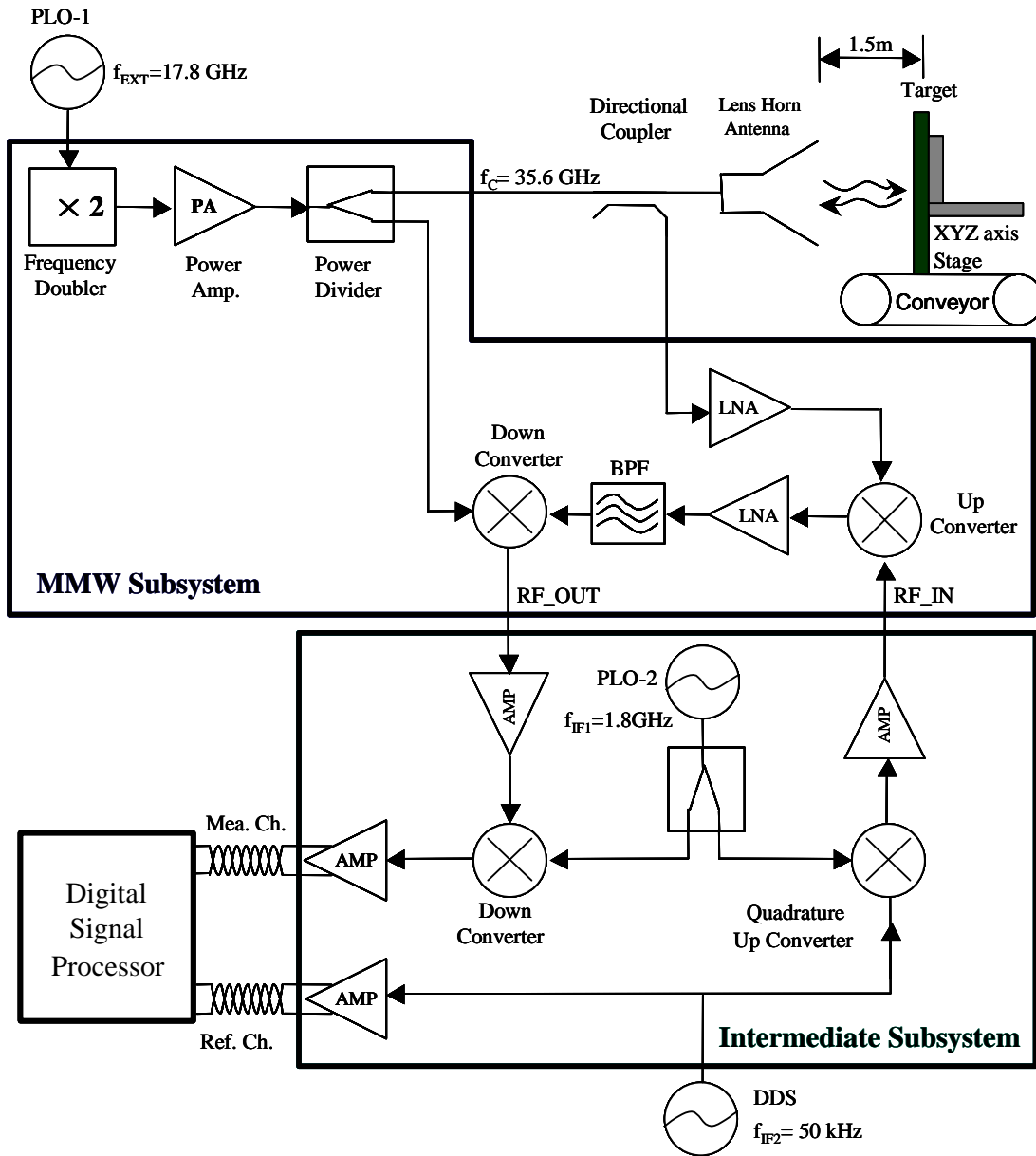


Fig. 4.1. Overall system block diagram. The target sits either on the XYZ axis (for displacement sensing) or on the conveyor (for velocity measurement). The Reference channel is not needed for velocity measurement.

4.1.1 Displacement measurement

Displacement of a target is measured by detecting the phase difference between the two base band signals: reference-channel signal $v_R(t)$ and measurement-channel signal $v_M(t)$. These signals are described as

$$\begin{aligned} v_R(t) &= A_R \sin[2\pi f_{IF2}t + \phi_R(t)] + n(t) \\ v_M(t) &= A_M \cos[2\pi f_{IF2}t + \phi_M(t) + \phi_n(t)] + n(t) \end{aligned} \quad (4.1)$$

where A_R , A_M and $\phi_R(t)$, $\phi_M(t)$ are the peak amplitudes and phases of these signals, respectively; $\phi_n(t)$ is the phase noise down-converted from the millimeter-wave signal; and $n(t)$ is the white Gaussian noise. The phase noise of the reference-channel signal is not considered here because its contribution is negligible as compared to that of the measurement-channel signal.

The phase of each channel's signal is obtained by the quadrature sampling signal processing and discussed in the following section. The phase difference between the channels, $\phi_D(t)$, is defined as

$$\phi_D(t) = \phi_M(t) - \phi_R(t) + \phi_n(t) \quad (4.2)$$

Here, we can consider only the phase noise, neglecting the white Gaussian noise, on the basis of the phase noise spectrum of the actual signals shown in Fig. 5.4 and obtained by the FFT spectral estimator¹ which indicates that phase noise is the dominant noise source in the frequency band of interest and is approximately greater than 30 dB from the noise floor.

The differential phase difference, needed for calculating the displacement, is obtained in the (digital) time domain as

¹ FFT spectral estimator is a signal processing based on FFT for generating the frequency spectrum of a signal.

$$\Delta\phi_D(nT) = \phi_D(nT) - \phi_D[(n-1)T] \quad n = 1, 2, 3, \dots \quad (4.3)$$

where T is a sampling time interval.

In the case of normal incidence of a wave, the range $r(t)$ from the antenna to the target is related to the phase detected $\phi(t)$ as

$$r(t) = \frac{\phi(t)}{4\pi} \lambda_0. \quad (4.4)$$

The displacement is given by

$$\Delta r(nT) = r[nT] - r[(n-1)T] \quad n = 1, 2, 3, \dots \quad (4.5)$$

which can be determined using (4.3) and (4.4). The total displacement of the entire target movement is a summation of consecutive displacements:

$$d(nT) = \sum_{n=1}^k \Delta r(nT) \quad n = 1, 2, 3, \dots, k. \quad (4.6)$$

4.1.2 Doppler velocimetry

The measurement-channel signal, $v_M(t)$, produced by the target in motion, is frequency-shifted in base band by the Doppler frequency, f_d , and can be expressed as

$$v_M(t) = A_M \cos[2\pi f_{IF2}t + 2\pi f_d t + \phi_n(t) + \phi_i] \quad (4.7)$$

where ϕ_i represents the deterministic phase constant.

The principle of radar velocimetry relies on the detection and estimation of the Doppler frequency generated by a moving target. For the normal incident wave, which is our interest, the Doppler frequency, is related to the target speed, v , and the wave length, λ , as

$$f_d = \frac{2v}{\lambda} \quad (4.8)$$

in which the target velocity is linearly proportional to the Doppler frequency. The Doppler frequency shift is obtained in base band with reference to the intermediate frequency, f_{IF2} , by taking gradient for time derivative of the detected phase over time.

4.2 Signal processing

The sensor's signal processing consists of two distinct parts: one for detecting the phase difference needed for measuring the displacement, and another one for estimating the Doppler frequency used for calculating the velocity.

4.2.1 Phase-difference detection for displacement measurement

Fig. 4.2 shows the signal processing flow to extract the phase difference between the measurement- and reference-channel signals in the digital signal processor. In the input signals, the subscripts + and – designate different polarities of the differential signals coming from the differential amplifier in the IF subsystem. The front-end differential amplifier installed in the data acquisition hardware not only amplifies the both input channel signals driven by the sensor, but also greatly suppresses the common mode noise with a more than 50-dB common mode rejection ratio, due to the inherent characteristic of a differential amplifier. The reference- and measurement-channel signals are converted into a digital form with 12-bit resolution by the analog-to-digital converter (ADC), implemented in the data acquisition hardware. These signals are expressed as

$$\begin{aligned} v_R(nT) &= A_R \sin[2\pi f_{IF2}(nT) + \phi_R(nT)] \\ v_M(nT) &= A_M \cos[2\pi f_{IF2}(nT) + \phi_M(nT) + \phi_n(nT)] \quad n = 1, 2, 3, \dots \end{aligned} \quad (4.9)$$

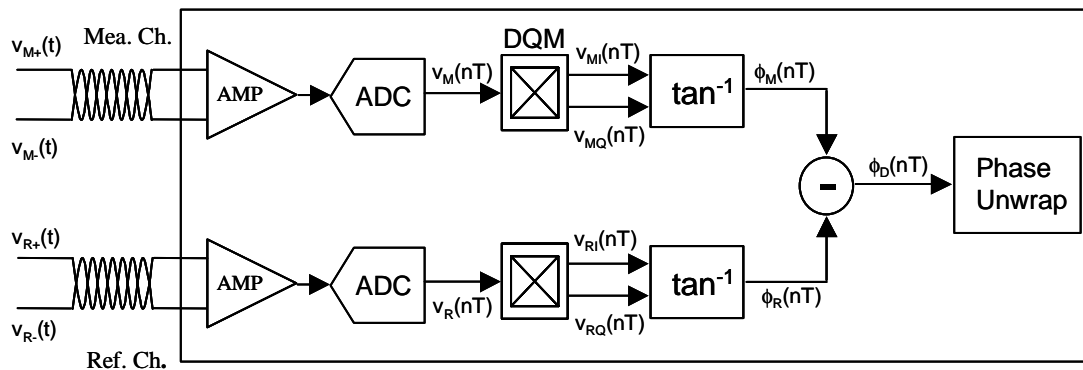


Fig. 4.2. Signal processing flow in the digital signal processor for displacement measurement.

A digital quadrature mixer (DQM), based on quadrature sampling signal processing technique was configured and implemented as shown in Fig. 4.3. Various quadrature sampling schemes have been proposed for coherent detection in radar and communication receivers [41]-[45]. The advantage of the quadrature sampling is that it can eliminate or, at least, minimize the non-linear phase response of a conventional analog quadrature mixer, which is caused by the phase and amplitude imbalances as well as the DC offset voltage of the mixer itself. As the operating frequency is increased, the non-linearity becomes severe and difficult to control. Several correction techniques have also been developed in [17]-[19]. The DQM implemented in our developed system was inspired by the work presented in [42],[44], and realized by software. The DQM processes each digitized channel signal to generate the in-phase and quadrature components of $v_{MI}(nT)$, $v_{MQ}(nT)$ and $v_{RI}(nT)$, $v_{RQ}(nT)$. The sampling frequency is set as four times the second intermediate frequency, $4f_{IF2}$, so that the digital local oscillators become a quadrature sequence of only -1, 0, and 1, which implies that local oscillators feed exactly 90 degrees out of phase and equal amplitude signals into the mixers, because their phases are integer multiple of $\pi/2$. The mixer designated in Fig. 4.3 performs as a multiplier. The multiplication process samples the following in-phase and quadrature components of the reference-channel signal [52]:

$$\begin{aligned}
 v_I(nT) &= \begin{cases} 0 & n = \text{odd} \\ I(nT) \cos \phi_i + Q(nT) \sin \phi_i & n = \text{even} \end{cases} \\
 v_Q(nT) &= \begin{cases} 0 & n = \text{even} \\ Q(nT) \cos \phi_i - I(nT) \sin \phi_i & n = \text{odd} \end{cases}
 \end{aligned} \tag{4.10}$$

where $I(nT) = A_R \cos \phi_R(nT)$, $Q(nT) = A_R \sin \phi_R(nT)$. ϕ_i is the initial phase, which is static in nature. As seen in (4.10), the odd samples of in-phase signal $v_I(nT)$ and the even samples of quadrature signal $v_I(nT)$ always produce zero, caused by multiplication with zero from digital oscillators, and they need to be discarded. Decimating by two

discards those samples to eliminate zero output in (4.11). In this quadrature sampling approach, a time delay in quadrature signal occurs because the first sample of $v_I(nT)$ produces zero and it is discarded. Therefore, adding a time delay of $\tau=1/4f_{IF2}$ to the in-phase signal eliminates the time delay between the two quadrature signals, $V_{RI}(nT)$ and $V_{RQ}(nT)$. Taking arctangent then produces the phase of each channel signal within 2π radians, $[-\pi, \pi]$, as

$$\phi_R(nT) = \tan^{-1} \left[\frac{v_{RI}(nT)}{v_{RQ}(nT)} \right]. \quad (4.11)$$

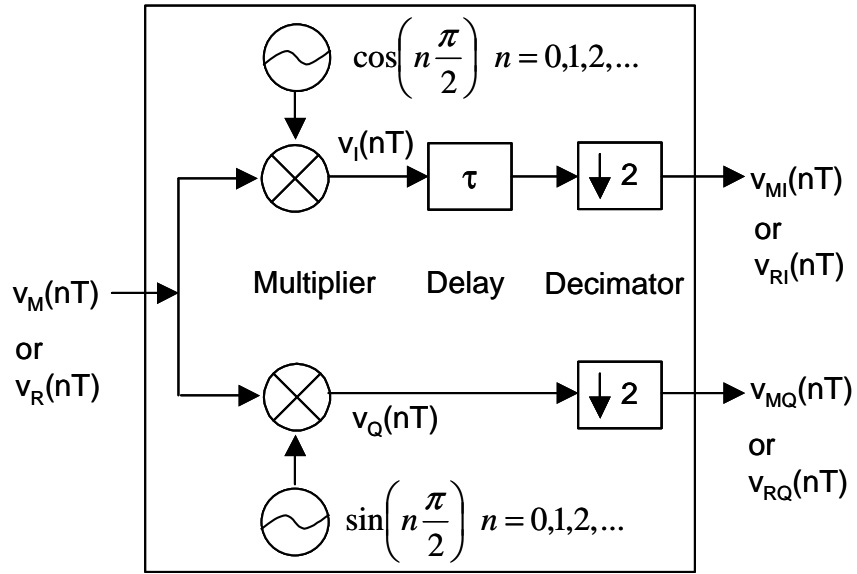


Fig. 4.3. Configuration of the digital quadrature mixer.

In this configuration, a low-pass filter is not needed for the rejection of the harmonics as in a typical mixer configuration, thus avoiding the filter's transient response to appear in the quadrature outputs, another advantage of our DQM approach.

For the measurement-channel signal, the same procedure is used to obtain

$$\phi_M(nT) = \tan^{-1} \left[\frac{v_{MI}(nT)}{v_{MQ}(nT)} \right]. \quad (4.12)$$

The phase difference, to be converted into displacement, is then determined as

$$\phi_D(nT) = \phi_M(nT) - \phi_R(nT) + \phi_n(nT). \quad (4.13)$$

Finally, the phase-unwrapping process [12]-[14], explained in 3.2, is applied to (4.13) to overcome the 2π -discontinuity problem of the phase detection processor. Then the range corresponding to the detected phase difference is determined by (4.4) and the displacement is obtained by equations (4.5) and (4.6).

4.2.2 Doppler-frequency estimation for velocity measurement

Fig. 4.4 depicts the signal processing flow used for estimating the Doppler frequency. The measurement-channel signal produced by a target in motion can be expressed, in digital form, as

$$v_M(nT) = A_M \cos[2\pi f_{IF2}(nT) + 2\pi f_d(nT) + \phi_n(nT) + \phi_i] \quad n=0,1,2, \dots, N-1 \quad (4.14)$$

A quadrature down-conversion by the DQM, combined with the phase-based frequency estimation shown in Fig. 4.4, allows low Doppler frequency to be measured with high resolution and directional information, regardless of the number of cycles of the Doppler frequency. A time-varying phase sequence, $\phi_M(nT)$, is generated from the down-converted quadrature signals, $v_{MI}(nT)$ and $v_{MQ}(nT)$. Taking arctangent gives the phase sequence of the down-converted measurement-channel signal within 2π radians,

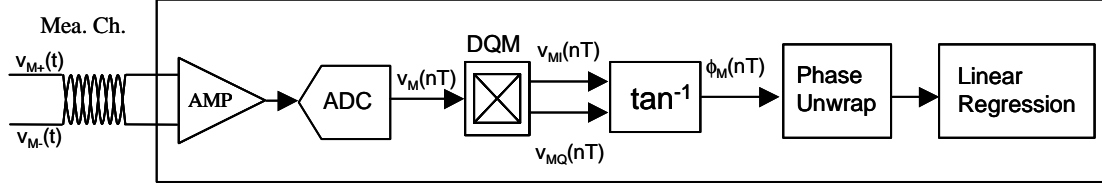


Fig. 4.4. Signal processing flow for velocity measurement.

$[-\pi, \pi]$, as

$$\phi_M(nT) = 2\pi f_d(nT) + \phi_n(nT) + \phi_i. \quad (4.15)$$

The phase unwrapping process is then applied to (4.15) to overcome the 2π -discontinuity problem of the phase detection processor. For velocity measurement, the Doppler frequency shift is estimated by applying the least squares or linear regression [46] over the unwrapped phase sequence of (4.15), from which target velocity can be calculated. This approach is, in principle, motivated by the work of Tretter [47]. The process of linear regression fits the unwrapped phase sequence, corrupted by phase noise, into a straight line, from which the Doppler frequency is obtained by taking gradient of the regression line. The phase locking of a microwave signal suppresses the $1/f$ noise component of a reference oscillator, typically a YIG oscillator, and allows the reference oscillator to follow the frequency characteristics of an internal or external frequency standard, usually a temperature-stabilized crystal oscillator, within the phase-locking frequency range. Thus the phase noise spectrum of a phase-locked microwave signal source shows a white Gaussian noise spectrum within the phase-locked bandwidth. In the data acquisition, the sampled data is affected mainly by the white noise down-converted from a microwave signal. Based on this fact, the problem of Doppler frequency estimation is transformed into the minimization of the square error [47], by fitting a linear line to $\phi_M(nT)$ corrupted with white Gaussian noise,

$$\varepsilon = \sum_{-(N-1)/2}^{(N-1)/2} \left\{ \phi_M(nT) - \left[2\pi \hat{f}_d(nT) + \hat{\phi}_i \right] \right\}^2 \quad (4.16)$$

where \hat{f}_d and $\hat{\phi}_i$ are the estimates of the Doppler frequency and phase constant, respectively, and N is a total sample number. Random process (noise) is generally treated with statistical analysis tools of mean, standard deviation, and variance. The corresponding theoretical lower limit of variance, Cramer-Rao Bound (CRB), for the frequency estimate \hat{f}_d is derived in [47] as

$$CRB(\hat{f}) = \frac{1}{2\pi} \frac{6}{SNR \cdot T^2 N(N^2 - 1)} \quad (4.17)$$

where high signal to noise ratio (SNR) is assumed, and phase noise is presumed as white. If the error in (4.16) is unbiased, which is valid for high signal-to-noise ratio, then the true Doppler frequency shift can be obtained as

$$f_d = E \left[\hat{f}_d \right] \quad (4.18)$$

where E denotes a statistical expectation or mean.

As an example, Fig. 4.5 illustrates the linear regression performed 10 times for the Doppler frequency of ± 1 Hz, generated by DDS, and $N=32$. The Doppler frequency is estimated from the gradient of each regression line from phase-time sequences, and the sign of the gradient determines the opening (receding) or closing (approaching) motion of a target.

The corresponding time response of DQM is shown in Fig. 4.6, which was deliberately acquired over many samples ($N=250,000$) to cover one period of the Doppler frequency of +1 Hz. In our sensor, however, the number of samples used for the linear regression frequency estimator is only a small fraction of that used for one period of the Doppler frequency. On the contrary, relatively large samples in FFT algorithm are required to detect a low-frequency sinusoid with high resolution as seen by the following relationship:

$$\Delta f = \frac{f_s}{N} \quad (4.19)$$

where Δf and f_s are the resolution and sampling frequency of FFT, respectively. In practice, it cooperates with maximum likelihood estimation (MLE) to maximize the resolution in FFT, which is composed of two steps: first, coarse spectral peak is determined by FFT; and second, fine peak is analyzed by introducing numerical technique like a center of gravity algorithm.

Comparison of the capability between the two different frequency estimators, FFT-based MLE and linear regression, is given in Fig. 4.7, which displays the histogram of the Doppler frequency estimates, iterated 10,000 times for the test signal generated by DDS, and shows the difference in statistical distribution of the estimate for the Doppler frequency of +1 Hz, with the same condition of $f_s=200$ kHz, $N=32$ and high SNR (70 dB). The variance of the frequency estimator is dependent on the number of samples, sampling time, and SNR of the sampled signal. Therefore, different conditions imposed on one of those parameters result in differences in estimation performance. In the comparison, the same conditions are exerted and only the high SNR case is considered because, in our sensor, it is easily realizable at f_{IF2} by cascading band-limited amplifiers without much increase in cost. The criterion of high SNR was referred to as 15 dB in [47]. As the figure indicates, the linear regression (on detected phase) shows a narrower statistical distribution, which implies a smaller variance of the estimated Doppler frequency.

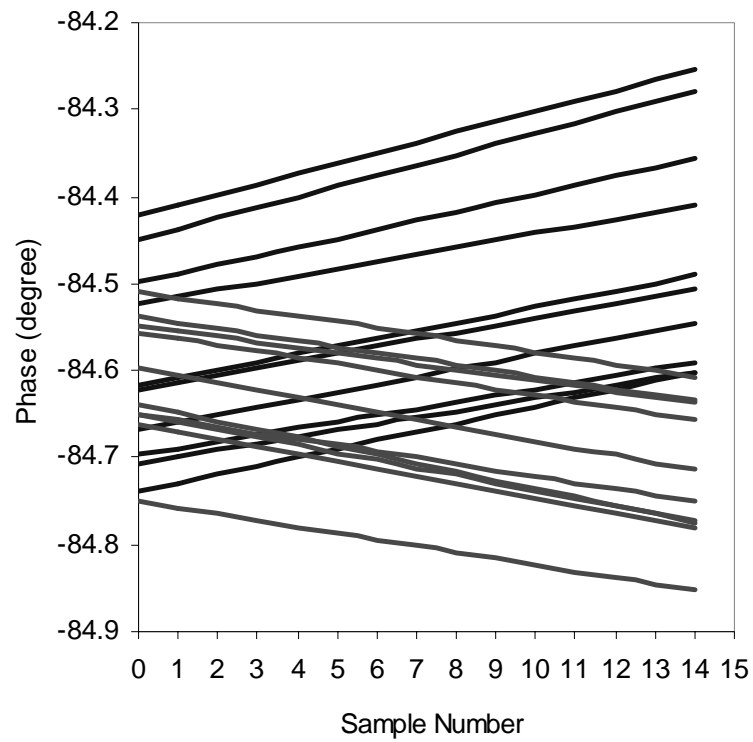


Fig. 4.5. Linear regression for the Doppler frequency of ± 1 Hz.

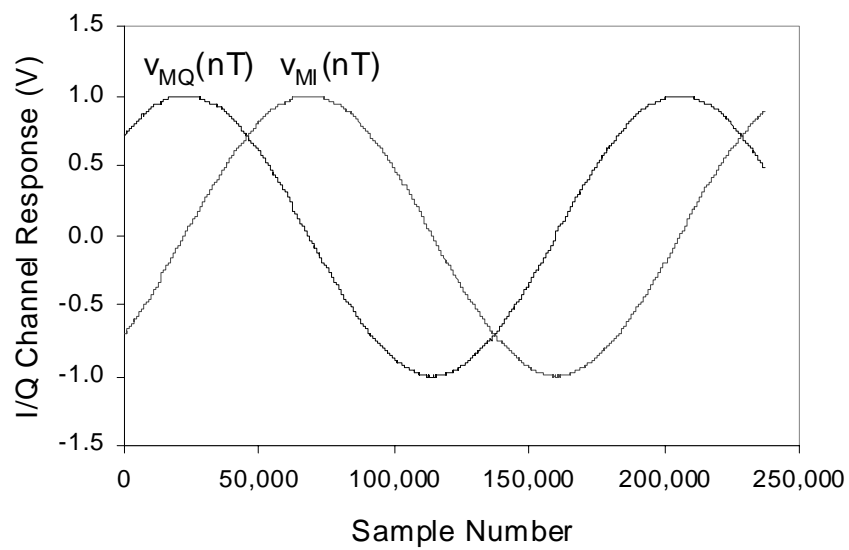


Fig. 4.6. Time response of the DQM for the Doppler frequency of $+1$ Hz.

In the FFT-based MLE, the Center of Gravity algorithm was used for determination of the spectral centroid [48]. As can be seen in Fig. 4.7, the linear regression frequency estimator provides better performance than the FFT-based MLE as long as high SNR is maintained.

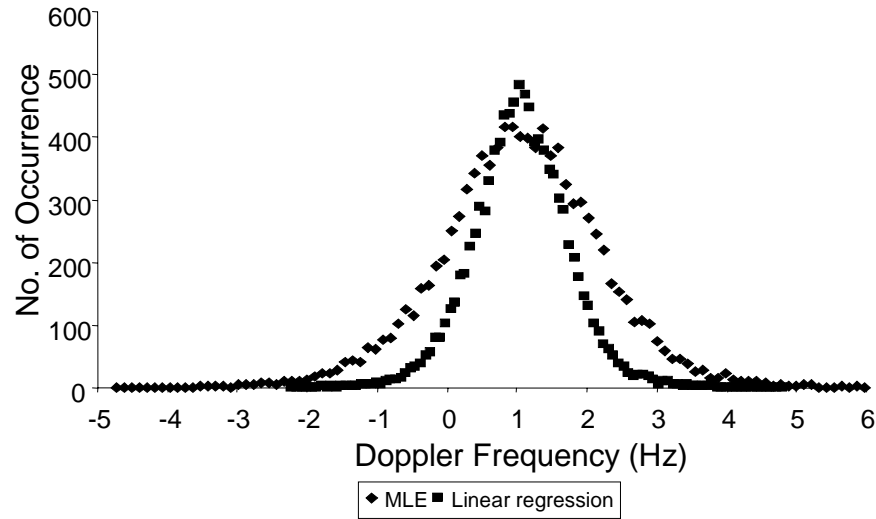


Fig. 4.7. Histogram of the estimated Doppler frequency using MLE and linear regression methods.

4.3 System fabrication and test

As seen in Fig. 4.1 and discussed previously, the sensor is divided into three parts. The millimeter-wave and intermediate-signal subsystems were realized using MICs and MMICs. The millimeter-wave subsystem was fabricated on a 0.25-mm-thick alumina substrate, as shown in Fig. 4.8 (a). The intermediate-signal subsystem was implemented on a FR-4 Printed Circuit Board (PCB), as shown in Fig. 4.8 (b). In the millimeter-wave subsystem, a Wilkinson power divider was designed to split the millimeter-wave signal into the transmit signal and the local oscillator signal for the down-converter. The band-pass filter is a coupled-line filter. It was designed for a 3-dB bandwidth of about 2 GHz at center frequency 36GHz using a field simulator, IE3D, and acts as an image-rejection filter. Details of the alumina circuit layout are shown in Fig. 4.9, where the metallization of a microstrip transmission line is composed of TiW(250Å), Ni(0.04mil), and Au(0.15mil) metal combination.

Commercially available Ka-band MMICs were used for the up-converter (Velocium, MSH108C), down-converter (Velocium, MDB162C), low noise amplifier (Velocium, ALH208C), power amplifier (TriQuint, TGA1071-EPU), and frequency doubler (TriQuint, TGC1430F-EPU). They are surface-mounted on metallic patches connected to the alumina substrate's ground plane by 0.2-mm-diameter vias. These chips were bonded to 0.25-mm-wide microstrip lines using gold ribbons.

In the intermediate-signal subsystem, a phase-locked oscillator operating at 1.8 GHz, designated by PLO-2 in Figs. 4.1 and 4.9(b), was designed using a phase-locked-loop frequency synthesizer (Analog Devices, ADF4113) which requires only a low-pass-loop filter as a external component, along with a voltage-controlled oscillator (Sirenza Microdevices, VCO190-1850T) and a 10-MHz oven-controlled crystal oscillator used as a frequency standard. A direct quadrature modulator (RFMD, RF2422) was used to generate a single sideband (SSB) signal that shifted the frequency f_{IF1} by f_{IF2} . The measured SSB signal shows carrier and sideband suppression of greater than 45 dB at the IF of 50 kHz, achieved by tuning the phase of the IF quadrature input signal. For the

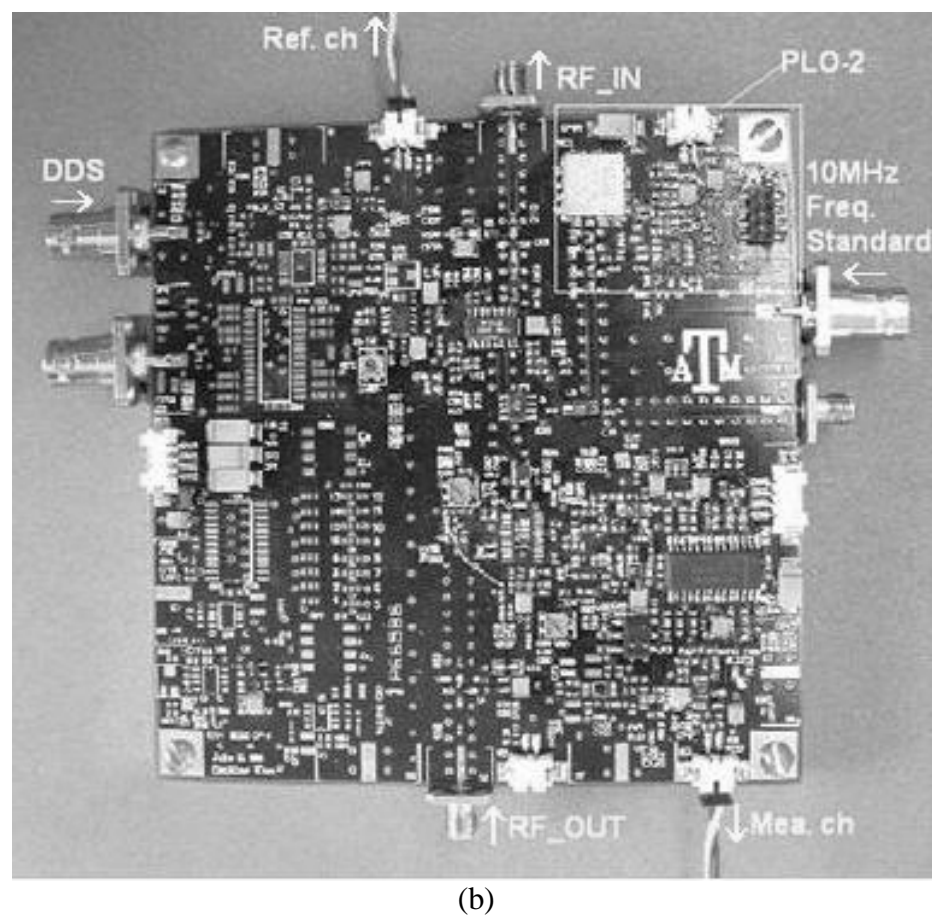
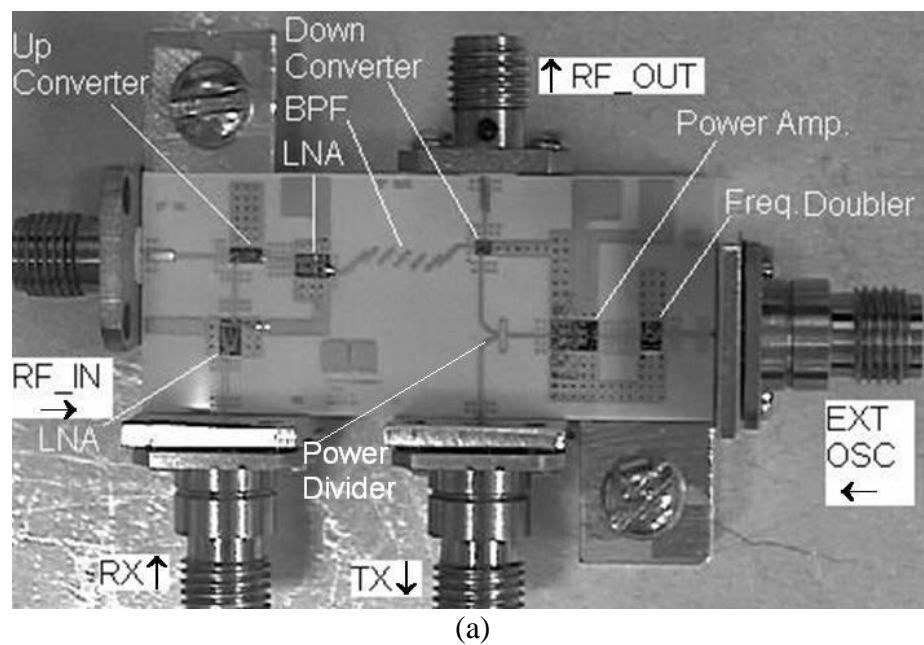


Fig. 4.8. Photograph of the fabricated millimeter-wave (a) and intermediate-signal (b) subsystems.

down-conversion, a direct quadrature demodulator (Analog Devices, AD8347) was utilized, and one of the quadrature output signals was served as the measurement-channel signal. The differential amplifiers, used for the measurement- and reference-channel signals, greatly suppress the common-mode noise, resulting in a common-mode rejection ratio² of more than 50 dB.

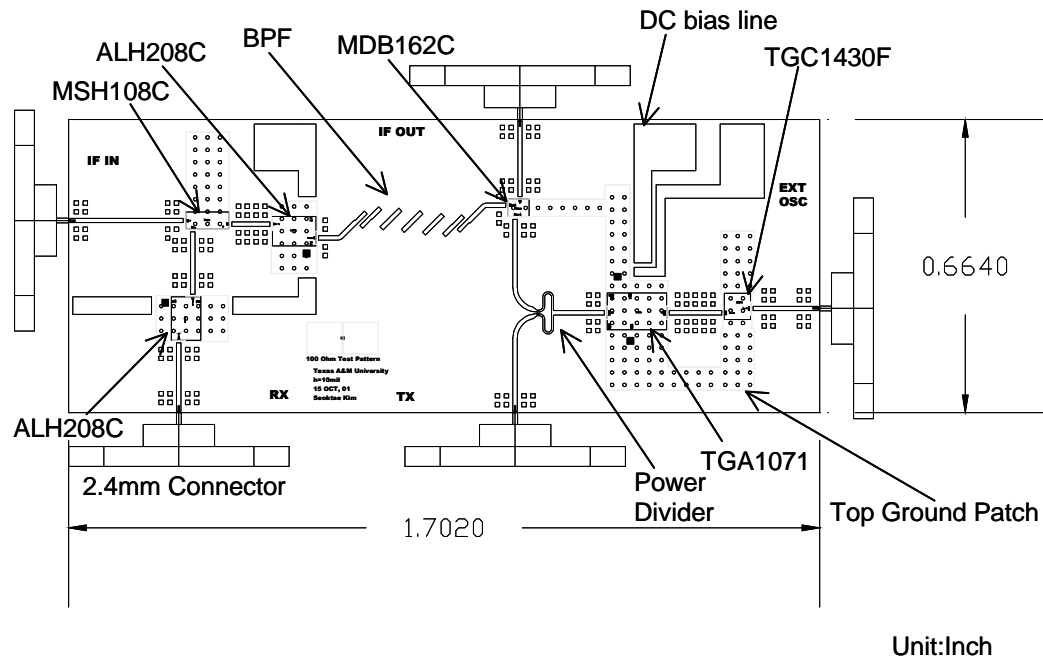


Fig. 4.9. Millimeter wave subsystem layout in detail.

² A measure of differential amplifier's ability to reject an undesired signal (noise) that is common to both inverting and non-inverting input terminals.

4.3.1 Displacement measurement results

The developed sensor was tested for measuring the displacement of a metal plate mounted on a XYZ axis stage. The stage has a precision of $10\text{ }\mu\text{m}$, an accuracy of $2.0\text{ }\mu\text{m}/25.4\text{ mm}$, and a repeatability of $1.27\text{ }\mu\text{m}$.

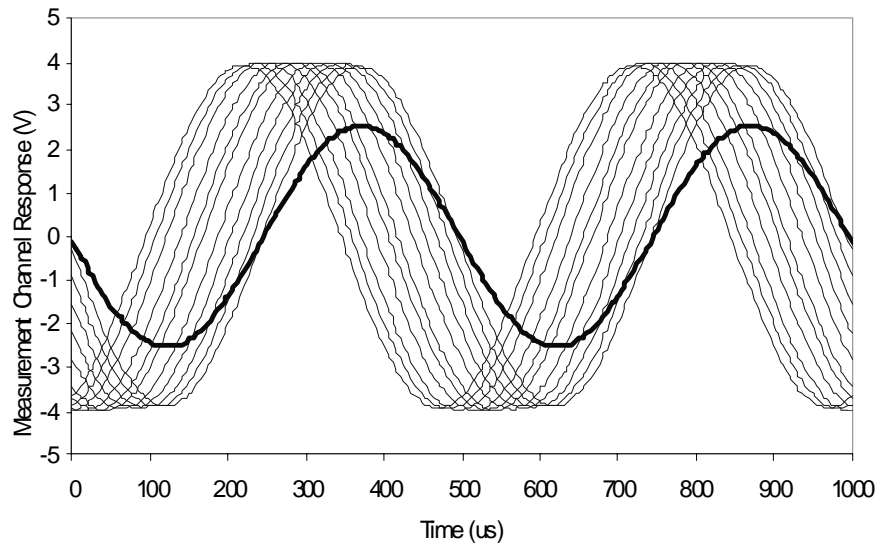


Fig. 4.10. Measurement-channel response for every $100\text{-}\mu\text{m}$ displacement. Thick solid line represents reference-channel signal.

The metal plate was located at 1.5 m away from the antenna aperture. The displacement was measured as the plate was moved every $100\text{ }\mu\text{m}$. For each measurement, the data acquisition board sampled 1,000 data points and averaged them to cancel out white noise components. Fig. 4.10 shows voltage response of the measurement-channel signal triggered with the reference-channel signal for every $100\text{-}\mu\text{m}$ displacement. The detected and unwrapped phases are shown in Fig. 4.11. The constructed displacement from the unwrapped phase is shown in Fig. 4.12, along with its error. It is interesting to note that the measured error is regular and periodic, indicating that multiple reflections between antenna and metal plate are predominantly attributed to

the error source; the multiple reflections are typically caused by the combination of mismatch at input junction of the antenna and re-radiation of reflected wave from the highly reflecting target from antenna aperture occurred typically in short distance. In order to improve the measurement accuracy, we introduced a polynomial curve fitting approach to correct for the error. The curve fit using polynomial series, y_i , is formed generally by

$$y_i = \sum_{j=0}^m a_j d_i \quad (4.20)$$

where d_i is the input displacement sequence, and a_j and m are the coefficients of the polynomial curve fit and polynomial order, respectively. In this curve-fitting process, the coefficients a_j are determined to minimize the mean square error (MSE),

$$MSE = \frac{1}{N} \sum_{i=0}^{N-1} (y_i - r_i)^2 \quad (4.21)$$

where r_i represents the measured input sequence, and N is number of the data points.

Fig. 4.13 shows the measured and curve-fitted errors with a polynomial order of 13 using SVD (Singular Value Decomposition) algorithm [49]. The displacement after correction along with the error, is shown in Fig. 4.14. A maximum error of 27 μm was obtained after the correction was made, a significant improvement from a maximum error of 281 μm without the correction as displayed in Fig. 4.12. Fig. 4.15 shows another measurement result demonstrating the achieved resolution. As shown, the measured maximum error distributes within 10 μm for the entire displacement of 300 μm . The result indicates that the smallest distance to discriminate two different positions of a target, resolution, is only 10 μm , which is equivalent to about $\lambda_0/840$. It should be mentioned here that in the last measurement, the XYZ axis stage was moved every 10 μm , which is the precision limit of the stage.

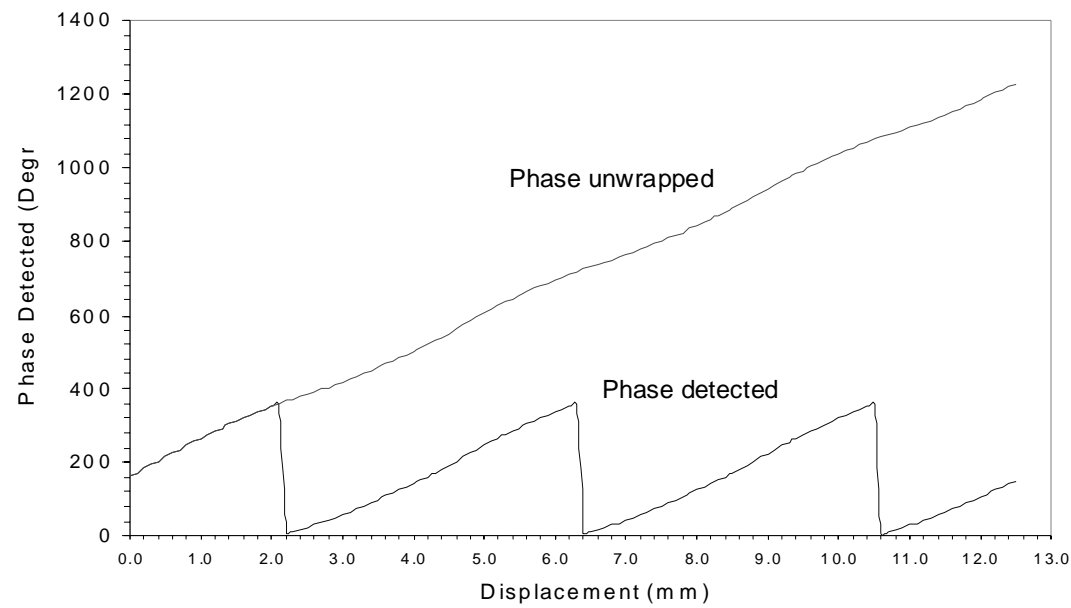


Fig. 4.11. Detected and unwrapped phase.

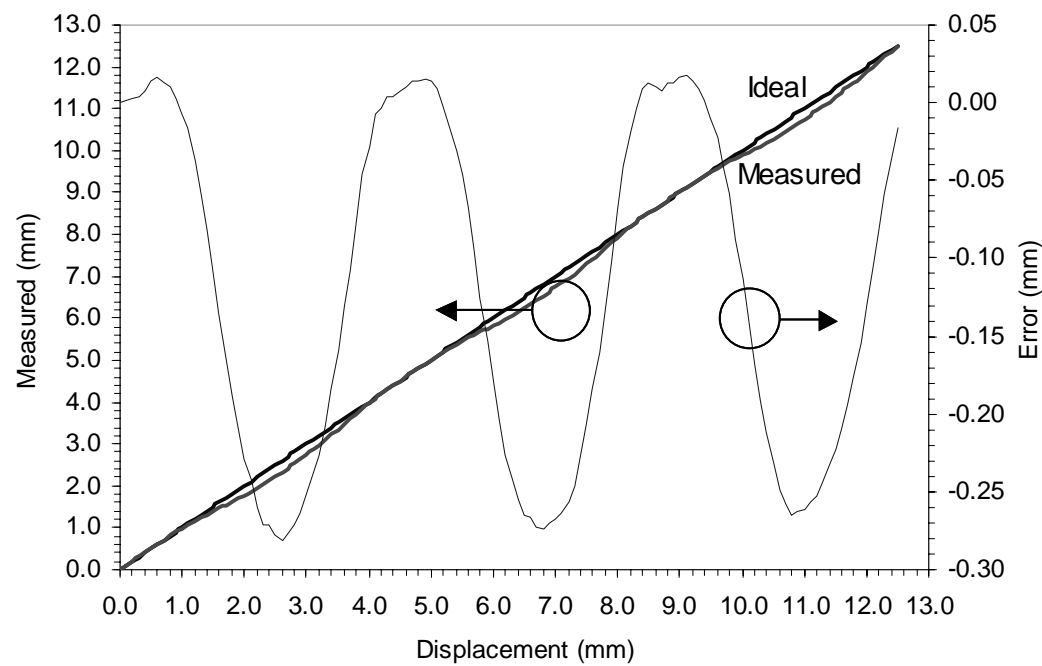


Fig. 4.12. Measured displacement and error for a metal plate.

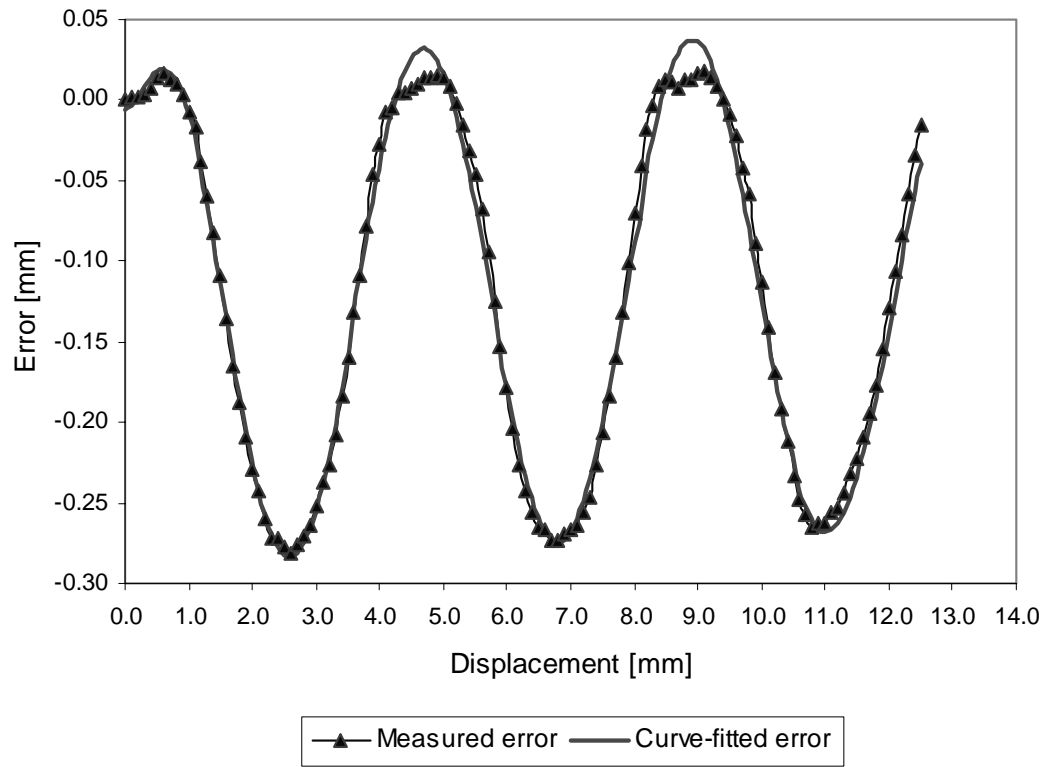


Fig. 4.13. Error correction by the polynomial curve fitting.

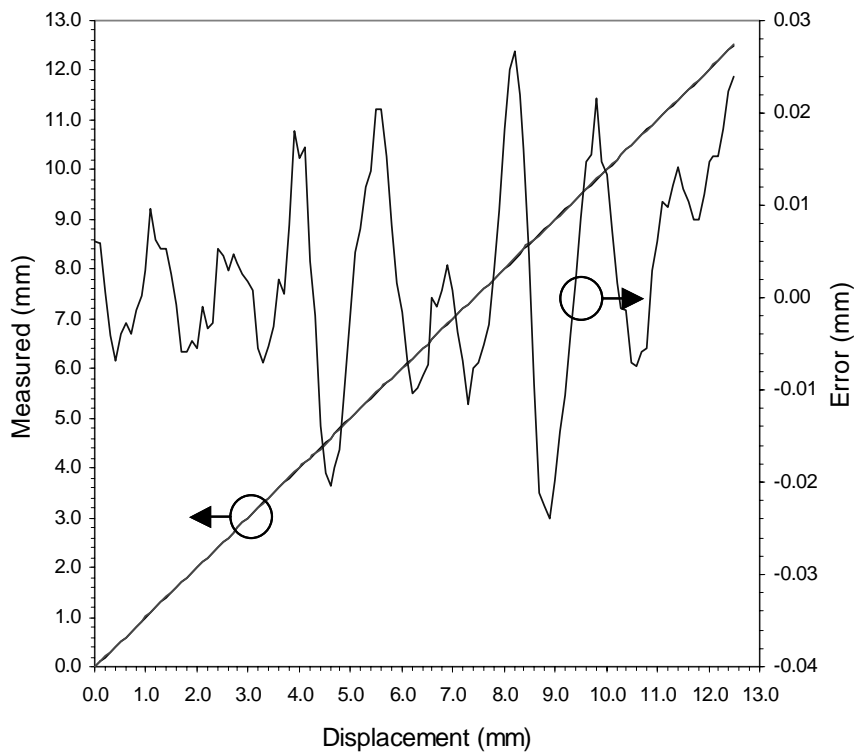


Fig. 4.14. Displacement results after error correction.

Thus, it is expected that part of the error in accuracy was due to the actual displacement of the stage, and a motorized stage would provide better reference for ideal displacement, leading to better accuracy.

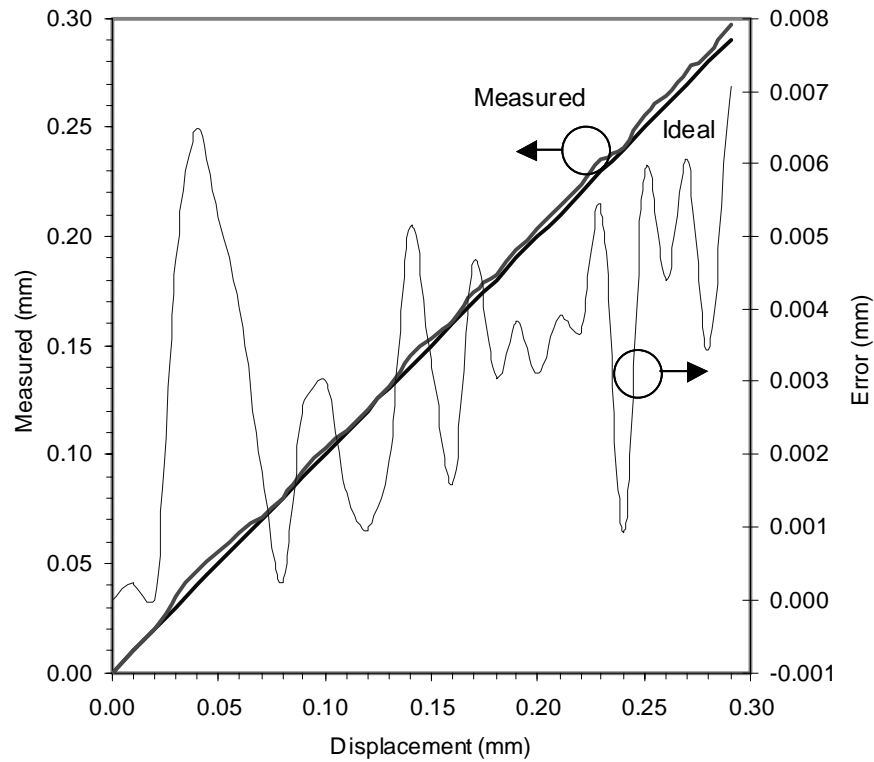


Fig. 4.15. Displacement measured every 10 μm .

4.3.2 Velocity measurement result

The test was done for the velocity of a closing target of metal plate, placed 1.5 m away from the sensor's antenna aperture, by varying the speed of the conveyor carrying the plate. The experimental results, shown in Fig. 4.16, were measured consecutively five times (represented by the measurement index), with N taken as 128. Each time, the measurement was repeated 200 times and the results were averaged. The variance of the Doppler frequency estimate for the averaged samples is then reduced by

$$\sigma_{avg}^2(\hat{f}_d) = \frac{\sigma^2(\hat{f}_d)}{N_{avg}} \quad (4.22)$$

where $\sigma^2(\hat{f}_d)$ is the variance of estimate for samples with $N=128$, and N_{avg} is the number of average; the standard deviation (σ) is a measure to characterize a random process with Gaussian distribution along with mean and variance; the number of the Doppler frequency estimate, which falls within $\pm 1\sigma$, is 68 percent of the total number of estimates. The mean values of measured velocity are 27.7, 32.6, and 38.6 mm/s for each different velocity. The corresponding standard deviation of the Doppler frequency estimates were calculated as 0.50, 0.61, and 0.64 Hz, respectively, from the statistical distribution of the estimates for each different velocity measurement with $N=128$ and $N_{avg}=200$. The velocity resolution is estimated as 2.7 mm/s by the maximum (worst) standard deviation of 0.64 Hz inferred from (4.22) and substituting it into equation (4.8) to convert into velocity.

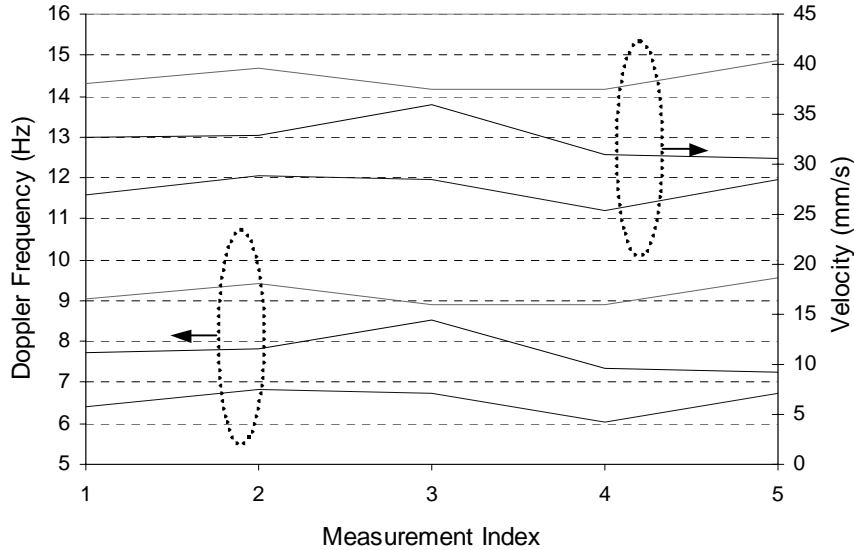


Fig. 4.16. Velocity measurement result for a closing target.

4.4 Summary

A new multi-function integrated-circuit millimeter-wave sensor operating at 35.6 GHz has been developed and demonstrated for displacement sensing, with micron resolution and accuracy, and for high-resolution low-velocity measurement. A digital quadrature mixer was introduced for a phase detection process, using a quadrature sampling signal processing technique, to overcome the general problem of non-linear phase response of a typically-employed conventional analog quadrature mixer. Displacement measurement results indicate that the sensor can detect the displacement as small as $10\text{ }\mu\text{m}$ or $\lambda_0/840$, representing the best-reported resolution in terms of wavelength in the millimeter wave range. Measurement error attributed to multiple reflections was corrected by polynomial curve fitting. After error correction, an unprecedented maximum measured error of only $27\text{ }\mu\text{m}$ has been achieved. Velocity as low as 27.7 mm/s , equivalent to 6.6 Hz in terms of Doppler frequency, has been measured at 35.6 GHz for a moving target. The velocity resolution is estimated as 2.7 mm/s . Much lower velocity and better resolution can be measured at the cost of computation and response time. Signal processing for Doppler frequency estimation was developed by means of linear regression on the detected phase combined with the quadrature down-conversion scheme, which provides high resolution and better performance compared to the conventional FFT-based MLE.

CHAPTER V

CONSIDERATION OF FREQUENCY STABILITY OF MICROWAVE SIGNAL SOURCE

5.1 Theoretical analysis of phase-noise effect on interferometric measurements

In this section, the effect of the frequency source's phase noise on the measurement with millimeter-wave interferometry is analyzed and investigated, using statistical analysis. It is shown that one can predict the stability requirement of the frequency source corresponding to the time delay between the transmit and receive signals. It is also demonstrated that the phase noise produces negligible effect on the phase measurement when the time delay is sufficiently small. The result is confirmed with the simulation of a representative millimeter-wave interferometric sensor for displacement measurement.

In an interferometer, the transmit signal from the source is mixed with the receive signal (obtained either by reflection from or transmission through the object) in a quadrature mixer to produce a base-band signal. This base-band signal corresponds to the phase difference (due to the time delay) between the transmit and receive signals and can be processed to produce the object information. Interferometry is basically a phase detection process and the measured phase error primarily dictates the accuracy of the target signature. The total induced phase error attributes to the combination of the quadrature mixer imbalance and frequency source instability during the phase detection process. The contribution from the quadrature mixer imbalance can be compensated by a correction algorithm in the signal processing as discussed in this dissertation, leaving the instability of the frequency source as the principal source of phase error.

In this section, the phase error induced by the instability or phase noise of the frequency source on millimeter-wave interferometric measurement is presented using statistical analysis, and it is demonstrated that this instability causes negligible effect on

the phase error when the time delay between the transmit and receive signals is relatively small.

The transmit and receive signals in an interferometric system can be described respectively as

$$v_T(t) = A_T [1 + m(t)] \cos[2\pi f_o t + \phi_n(t) + \phi_i] \quad (5.1)$$

$$v_R(t) = A_R [1 + m(t - t_d)] \cos[2\pi f_o (t - t_d) + \phi_n(t - t_d) + \phi_i] \quad (5.2)$$

where A_T and A_R are the amplitudes of the transmit and receive signals, respectively; $m(t)$ and $\phi_n(t)$ designate the AM (amplitude modulation) and PM (phase modulation) noise effects, respectively; ϕ_i is the initial phase of the frequency source, which can be considered as a constant; and t_d is the time delay between the transmit and receive signals. The effect of the AM noise on the phase detection is generally much smaller than that of the PM noise. Furthermore, in typical balanced quadrature mixers, the AM noise is suppressed by at least 20 dB. Thus, it is reasonable to neglect the AM noise contribution in the estimation of the induced phase error in microwave interferometers.

The in-phase and quadrature output signals of the quadrature mixer, after low-pass filtering, are given by

$$v_I(t) = A_I \cos[\Delta\phi_n(t) + \phi_S] + n(t) \quad (5.3)$$

and

$$v_Q(t) = A_Q \cos[\Delta\phi_n(t) + \phi_S] + n(t) \quad (5.4)$$

respectively, where $\Delta\phi_n(t) = \phi_n(t) - \phi_n(t - t_d)$ represents the phase error due to the phase noise of the source; $\phi_S = 2\pi f_o t_d$ is the (constant) phase difference between the transmit and receive signals corresponding to the time delay t_d ; and $n(t)$ stands for

additional noise from the receiver, which can be reduced significantly by averaging the digitized data by data acquisition hardware, in the signal processing, making its impact on the system performance negligibly small. The most important contribution to the phase error in the phase detection process is $\Delta\phi_n(t)$. The accuracy of the phase detection is degraded by the this noise term, which has uncertainty due to the random nature of noise. It is thus desirable to reduce or eliminate this phase noise effect in measurement. In the following, we will show that this phase noise effect can be neglected when the time delay between the transmit and receive signals is short.

The phase noise $\phi_n(t)$ in a frequency source is generally modeled by the Wiener process [50]-[51] as a quantity whose time-derivative is zero-mean white Gaussian frequency noise $f_n(t)$. The variance of phase deviation is derived as [52]

$$\sigma^2[\phi_n(\tau)] = E[\phi_n^2(\tau)] - E^2[\phi_n(\tau)] = (2\pi)^2 N_o \tau \quad (5.5)$$

where E denotes the mathematical expectation and N_o is the two-sided frequency noise power spectral density (PSD).

A millimeter-wave source corrupted by phase noise can be represented by

$$v(t) = A \cdot \cos[2\pi f_o t + \phi_n(t) + \theta] \quad (5.6)$$

where A is the maximum amplitude; f_o is the operating frequency; $\phi_n(t)$ is the phase noise; and θ is a random variable, which is uniform over $[0, 2\pi]$ and independent of $\phi_n(t)$. θ makes $v(t)$ stationary so that we can define the autocorrelation of $v(t)$ as

$$R_v(\tau) = E\{v(t)v^*(t+\tau)\} = \frac{A^2}{2} \operatorname{Re} \left\{ e^{j2\pi f_o \tau} e^{-\frac{(2\pi)^2}{2} N_o \tau} \right\} \quad (5.7)$$

The power spectral density is obtained as Fourier transform of the autocorrelation, according to Wiener-Khinchin theorem [52], as

$$S_v(\omega) = \int_{-\infty}^{\infty} R_v(\tau) e^{-j\omega\tau} d\tau = \frac{A^2}{2\pi^2 N_o} \left\{ 1 + \left(\frac{\omega - \omega_o}{2\pi^2 N_o} \right)^2 \right\}^{-1} \quad (5.8)$$

where $\omega_o = 2\pi f_o$ is the radian frequency of the source. N_o can be derived from (5.8) as

$$N_o = \frac{\Delta f}{2\pi} \quad (5.9)$$

where Δf is the 3-dB bandwidth of the power spectrum. Substituting (5.9) into (5.5) yields

$$\sigma^2[\phi_n(\tau)] = 2\pi\Delta f\tau \quad (5.10)$$

which implies that the mean square phase deviation is linearly proportional to the time difference τ , as expected for the Wiener process.

As stated earlier, the time derivative of $\phi_n(t)$ is zero mean, white Gaussian frequency noise, which is a wide-sense stationary (WSS) process. Then, $\Delta\phi_n(t)$ is also WSS. Thus we can define the autocorrelation of $\Delta\phi_n(t)$ as

$$R_{\Delta\phi_n}(\tau) = E\{\Delta\phi_n(t)\Delta\phi_n(t+\tau)\} = 2R_{\phi_n}(\tau) - R_{\phi_n}(\tau+t_d) - R_{\phi_n}(\tau-t_d) \quad (5.11)$$

The power spectral density corresponding to $R_{\Delta\phi_n}(\tau)$ can be derived using (5.8) as

$$S_{\Delta\phi_n}(\omega) = 2S_{\phi_n}(\omega)(1 - \cos \omega t_d) = t_d^2 \omega^2 S_{\phi_n}(\omega) \left(\frac{\sin \omega t_d / 2}{\omega t_d / 2} \right)^2 \quad (5.12)$$

where $S_{\phi_n}(\omega)$ is the power spectral density for $\phi_n(t)$. The power spectral density corresponding to the derivative of $\phi_n(t)$ is given as [53]

$$S_{\dot{\phi}_n}(\omega) = \omega^2 S_{\phi_n}(\omega) \quad (5.13)$$

One can rewrite (5.12), upon using (5.13), as

$$S_{\Delta\phi_n}(\omega) = t_d^2 S_{\dot{\phi}_n}(\omega) \left(\frac{\sin \omega t_d / 2}{\omega t_d / 2} \right)^2 \quad (5.14)$$

$\Delta\phi_n(t)$ is a zero mean stationary process, and its variance is computed by

$$\sigma^2[\Delta\phi_n(t)] = R_{\Delta\phi_n}(0) = \frac{t_d^2}{\pi} \int_0^\infty S_{\dot{\phi}_n}(\omega) \left(\frac{\sin \omega t_d / 2}{\omega t_d / 2} \right)^2 d\omega \quad (5.15)$$

As can be seen from (5.15), the mean square deviation of the phase noise, $\sigma^2[\Delta\phi_n(t)]$, relates to the frequency noise PSD of the frequency source, $S_{\dot{\phi}_n}(\omega)$, which can be

measured using a spectrum analyzer. The standard deviation or root mean square (rms) value of $\Delta\phi_n(t)$ is considered as the phase error; i.e. the phase deviation for the delay time t_d due to the phase noise of the frequency source. For the case when $S_{\dot{\phi}_n}(\omega)$ is

strictly white noise, (5.15) becomes

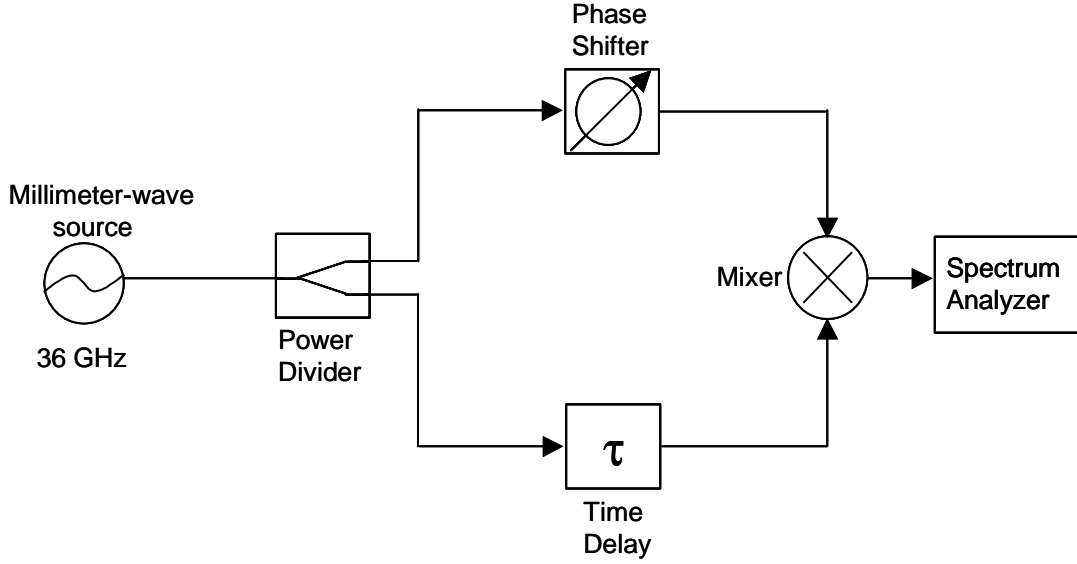


Fig. 5.1. Schematic representing the operation of a typical homodyne interferometer.

$$\sigma^2[\Delta\phi_n(t)] = 2\pi\Delta f\tau \quad (5.16)$$

which is the same as (5.10), after changing t_d to τ without loss of generality. Equation (5.16) allows one to determine the frequency source's stability requirement for a specific time delay to produce negligible phase error. For interferometric measurement with short time delay (e.g., $\tau < 10$ nS), the frequency source instability causes negligible phase error. Note that this conclusion is based on the assumption that the frequency noise PSD is white. Typical frequency noise PSD of a frequency source is not strictly white over the entire frequency range due to the random walk and flicker noise located close to the operating frequency. The assumption of white frequency source PSD, however, is justified when the time delay is short. To illustrate this, we consider a schematic shown in Fig. 5.1, which represents the operation of a typical homodyne interferometer.

The output voltage of the oscillator can be modeled as

$$v_s(t) = V_p \cos \left\{ 2\pi f_o t + \left[\sum_{m=1}^N \frac{\Delta f_p}{f_m} \sin(2\pi f_m t + \theta) \right] \right\} \quad (5.17)$$

where V_p is the maximum voltage amplitude; f_m is the offset frequency from the carrier; N represents the number of offset frequency terms used in the phase noise data; Δf_p is the peak frequency deviation resulting from the frequency noise; and θ is uniformly distributed over $[0, 2\pi]$. When the two input signals to the mixer are quadrature in phase, the output signal of the mixer at an offset frequency can be derived from Fig. 5.1 as

$$v_o(t) = K \sin \left(\frac{2\Delta f_p}{f_m} \right) \sin(\pi f_m \tau) \cos \left\{ 2\pi f_m \left[t - \left(\frac{\tau}{2} \right) \right] \right\} \quad (5.18)$$

where K measures the change of the mixer's output voltage due to change in the frequency noise. For the typical case of $\Delta f_p \ll f_m$ and when $f_m \ll \frac{1}{\tau}$ (for short time delay), (5.18) reduces to

$$v_o(t) = 2\pi K \Delta f_p \tau \cos \left\{ 2\pi f_m \left[t - \left(\frac{\tau}{2} \right) \right] \right\} \quad (5.19)$$

which implies that the output voltage from the mixer at an offset frequency is linearly proportional to the frequency noise. Also, (5.19) shows that the frequency noise may produce negligible voltage from the mixer when the time delay is sufficiently short. To confirm this phenomenon, we show in Fig. 5.2 the frequency noise PSD at the mixer's output as a function of offset frequency for different delay times calculated by HP ADS [54]. Typical phase noise of a Ka-band oscillator was used for the 36-GHz millimeter-wave source. The power divider, mixer, phase shifter and delay line were ideal components taken from the Agilent ADS library. As can be seen, the shorter the time

delay, the greater suppression of the frequency noise components at the low frequency offset in base-band. It is therefore reasonable to approximate that $S_{\phi_n}(\omega)$ is white for

short time delay. As an example, we consider a millimeter-wave interferometric sensor shown in Fig. 3.1 for displacement measurement. The range from the antenna to the target for normal incidence of wave relates to the detected phase difference $\phi(t)$ as

$$r(t) = \frac{\phi(t)}{4\pi} \lambda_0 \quad (5.20)$$

where λ_0 is the operating wavelength in air. The range variation is produced by changes in the surface profile and can be represented in the time domain as

$$r(nT) = r(nT) - r[(n-1)T] \quad n = 1, 2, 3, \dots \quad (5.21)$$

where T is the sampling interval. The displacement can be described as a summation of consecutive range variations:

$$d(nT) = \sum_{n=1}^k r(nT) \quad n = 1, 2, 3, \dots, k \quad (5.22)$$

Error in phase measurement thus produces displacement error through (5.20). Fig. 5.3 shows the rms value of the displacement error at 36 GHz as a function of time delay for various 3-dB bandwidths of the frequency source. From Fig. 5.3, we can deduce that the phase noise of the frequency source has little impact on the coherent phase detection using the interferometer for short time delay.

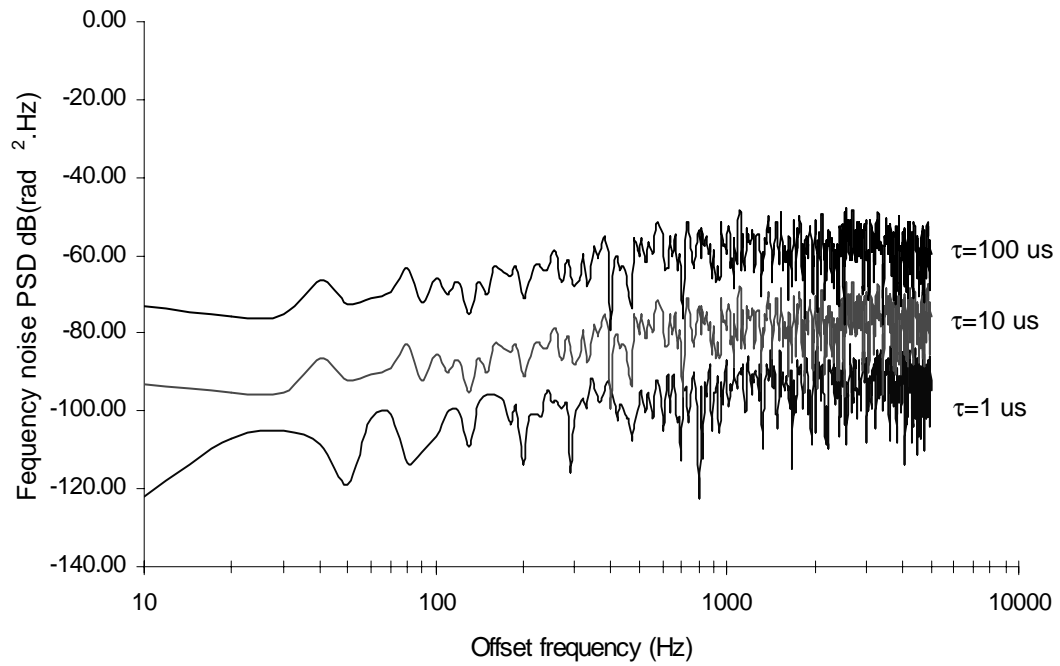


Fig. 5.2. Calculated time delay effect on the frequency noise PSD.

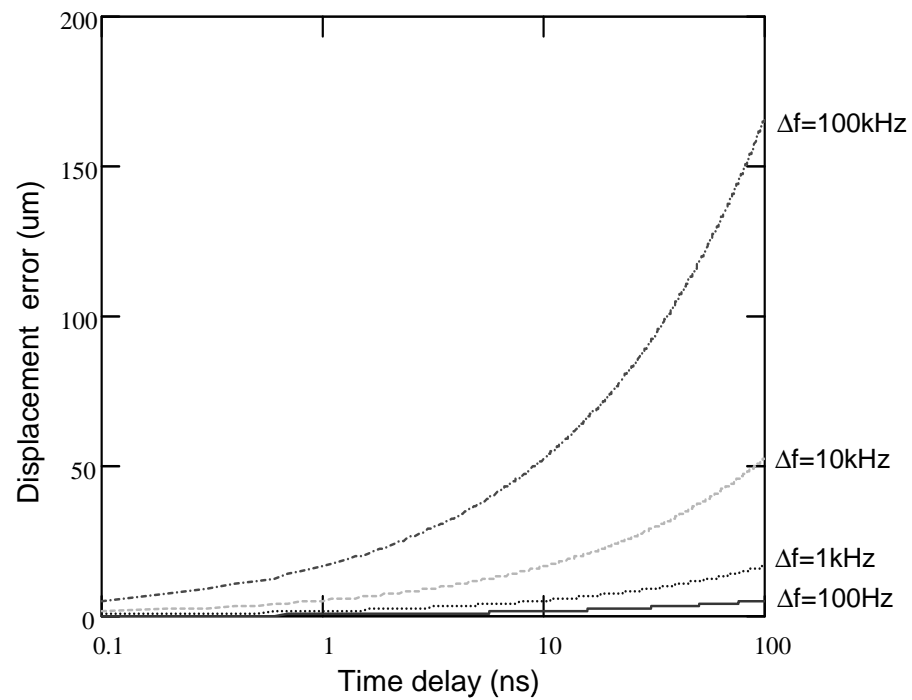


Fig. 5.3. rms displacement error of millimeter-wave interferometer operating at 36-GHz.

5.2 Phase noise estimation

Frequency instability of a microwave signal source contributes to the error that affects measurement accuracy. It is typically characterized by a phase noise spectrum in the frequency domain, or Allan variance in the time domain [55]. In our system, the phase noise of the millimeter-wave signal is down-converted and appears in the second IF signal, whose frequency is low enough to be manipulated by digital signal processing. We estimated the phase noise of the signal source through a phase noise spectrum obtained by the FFT spectral estimator, as shown in Fig. 5.4, for the actual measurement- and reference-channel signals. In the phase noise spectrum, the sampling frequency was chosen as 200 kHz with $N=4096$, and a Hanning window was used. Each spectrum was measured 50 times and then averaged.

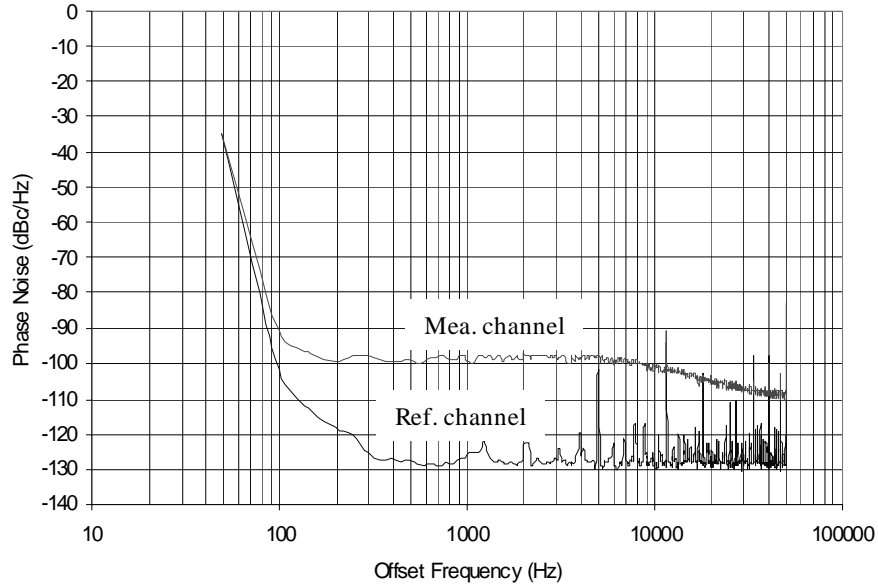


Fig. 5.4. Phase-noise spectrum of each channel.

A signal containing amplitude and phase noise can be represented, neglecting the inter-modulation of the amplitude and phase noise due to nonlinearity of the signal source or the components following it, as

$$v(t) = [A_p + a(t)] [\cos 2\pi f_c t + \phi_n(t)] \quad (5.23)$$

where $a(t)$ and $\phi_n(t)$ denote the respective amplitude and phase noise, and A_p and f_c are the amplitude and frequency of the signal, respectively. The double side-band power spectrum of (5.23) is a superposition of the carrier power and power spectrum of the amplitude and phase noise. That is,

$$S(f) = \frac{A_p^2}{2} \delta(f - f_c) + S_a(f - f_c) + S_\phi(f - f_c) \quad (5.24)$$

where δ is the Dirac delta function, and the second and third term represent the amplitude and phase noise power spectra, respectively. For a signal where external additive noise is predominant, as assumed for the reference-channel signal in our system, the power spectrum has equal contribution from the amplitude and phase noise [56]-[57]. The phase noise spectrum is thus 3 dB below the power spectrum normalized to the carrier power in a 1-Hz bandwidth. For the measurement-channel signal, the noise components of the signal are down-converted from the microwave signal source and governed by it. The spectrum of a microwave signal is typically dominated by the phase (or frequency) noise for the frequencies close to the carrier, and by amplitude noise for the frequencies more than a few tens of kHz from the carrier [58]. From this rationale, we can then neglect the contribution of the amplitude noise for the measurement-channel signal because we are interested only in the frequencies close to the carrier for phase

noise estimation. If we model the sinusoidal signal corrupted by phase noise as a linear frequency modulation process, then the signal is described as

$$v(t) = A_P \cos[2\pi f_c t + \eta(f_i) \sin(2\pi f_i t)] \quad (5.25)$$

where f_i is the modulating frequency, and $\eta(f_i)$ is the modulation index defined by

$$\eta(f_i) = \frac{\delta f}{f_i} \quad (5.26)$$

with δf being the peak frequency deviation at the modulating frequency f_i due to the frequency instability of the signal source. The phase noise spectrum of the signal can be approximated as power spectral density normalized to carrier power when the amplitude noise contribution is negligible. The single sideband (SSB) phase noise power $P_{ssb}(f_i)$ at an offset (or modulating) frequency f_i is related to the signal power, P_c , and the root mean square of the modulation index, η_{rms} , as

$$\frac{P_{ssb}(f_i)}{P_c} = \frac{\eta_{rms}^2(f_i)}{2}. \quad (5.27)$$

The SSB phase noise, in dBc/Hz, can be obtained by

$$L(f_i) = P_{ssb}(f_i) - RBW - P_C \quad (5.28)$$

where RBW represents the resolution bandwidth in dB, and the power is measured in dBm. Then the integrated phase noise variance is expressed as

$$\overline{\sigma_\phi^2} = 2 \int_{f_L}^{f_H} L(f_i) df_i \quad rad^2(dB) \quad (5.29)$$

where the bar denotes statistical average, f_H is defined as the upper-band limit of the band-limited differential amplifier of the sensor, and f_L is determined from the total observation time, NT , as

$$f_L = \frac{1}{2NT} \quad (5.30)$$

with N being the number of data points and T being the sampling time. On the basis of the fact that frequency is time derivative of phase given as

$$f(t) = \frac{1}{2\pi} \frac{d\phi(t)}{dt} \quad (5.31)$$

the power spectrum pair of the frequency and phase functions has the following relationship:

$$S_f(f) = (2\pi f)^2 S_\phi(f). \quad (5.32)$$

The variance of frequency noise over the same bandwidth can be obtained, making use of (5.29) and (5.32), as

$$\overline{\sigma_f^2} = 2 \int_{f_L}^{f_H} L(f_i) f_i^2 df_i \quad \text{Hz}^2(\text{dB}). \quad (5.33)$$

If the phase noise is white over the bandwidth, with the frequency noise spectrum having a rising slope of 20 dB/decade with increasing frequency, then (5.29) can be simplified to

$$\overline{\sigma_\phi^2} = 2[L(f_i)(f_H - f_L)] \quad \text{rad}^2(\text{dB}) \quad (5.34)$$

and (5.33) reduces to

$$\overline{\sigma_f^2} = 2 \left[L(f_i) \left(\frac{f_H^3 - f_L^3}{3} \right) \right] \quad \text{Hz}^2(\text{dB}) \quad (5.35)$$

The probability distribution and density functions of the phase difference defined by (4.13) are illustrated in Fig. 5.5, which shows the characteristics of Gaussian distribution. These results demonstrate that the phase noise process can be approximated as white Gaussian noise process over the bandwidth of (5.29). They were obtained by sampling 2000 data points and averaging 50 times.

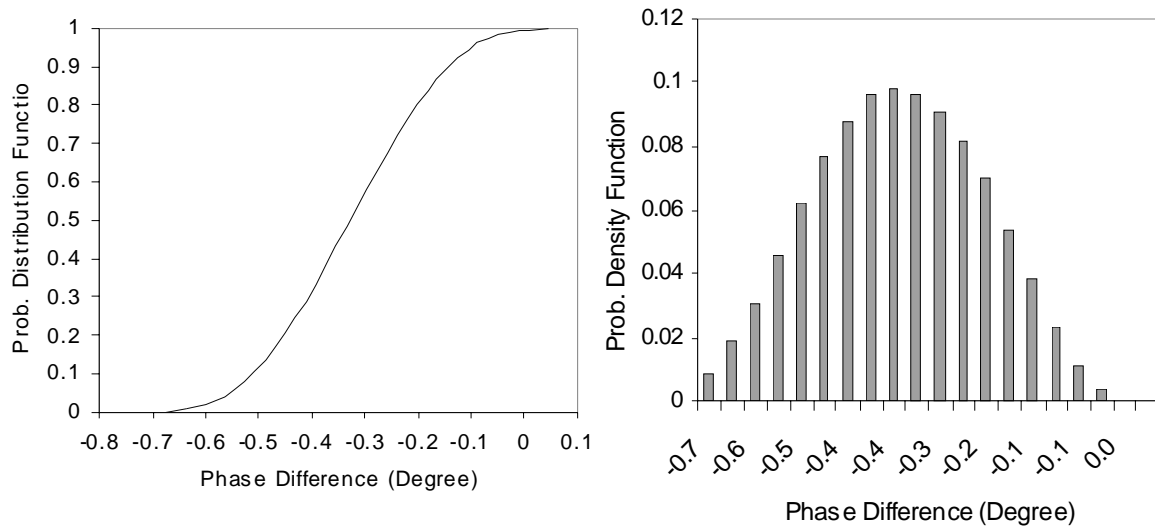


Fig. 5.5. Probability distribution function (a) and probability density function (b) for the phase difference.

Therefore, it is possible to determine the root mean square (rms) phase and frequency error originated from the instability of the frequency source by (5.34) and (5.35), respectively. The rms phase error was estimated as 0.13 degree for the measurement-channel signal, by substituting $f_H=9.81$ kHz and $f_L=100$ Hz into (5.34). For the reference channel, the error was obtained as 0.004 degree. The contribution of the frequency-source instability coming from DDS to phase error is therefore negligible. The rms frequency error estimated by (5.35) was 12.6 Hz for the same f_H with $f_L=781$ Hz.

CHAPTER VI

CONCLUSION

Millimeter wave interferometric sensors have been studied for industrial sensing applications. Two types of configuration were considered to implement the sensor: homodyne and double-channel homodyne. Both sensors were integrated on a planar structure using MMIC and MIC technology for light, compact, and low cost design, excluding some external components (phase-locked oscillator, directional coupler, and horn antenna). Homodyne configuration can be generally accepted for most sensing applications. Displacement measurement results show that sub-millimeter resolution in the order of 0.05 mm is feasible without correcting the non-linear phase response of quadrature mixer.

It becomes possible to exclude the non-linearity of the quadrature mixer and to estimate the frequency stability of a microwave signal source by means of the double-channel homodyne configuration, at the loss of a slight increase of circuit complexity. Also, the double-channel homodyne sensor provides better resolution of 0.01mm than the simple homodyne configuration. A digital quadrature mixer is constituted by a quadrature-sampling signal processing technique and claims for the elimination of a conventional quadrature mixer's nonlinear phase response.

Short-term stability of a microwave signal source was also considered through a phase noise spectrum obtained by a FFT spectral estimator, approximating the phase noise process as white Gaussian noise over the bandwidth of interest. The developed sensor demonstrates that displacement sensing with micron resolution and accuracy and high-resolution low-velocity measurement are feasible using millimeter-wave interferometer, which is attractive not only for displacement and velocity measurement, but also for other industrial sensing applications requiring very fine resolution and accuracy.

Through this research, it has been found that millimeter wave interferometry has a strong potential for industrial sensing applications requiring high resolution in the order

of sub-millimeter and fast response, and for replacement of laser interferometers used in a harsh working environment with dust, smoke, fog, and even danger of explosion. In this research, single-frequency interferometry is considered only for displacement measurement, liquid-level gauging, and velocimetry. But diversifying a system configuration makes it possible to bring forth diverse applications as optical interferometry, where much diversity is found in the number of beam, frequency source used, wave propagation medium, etc., for various applications such as length measurement, machine control, refractometry, microscopy and optical testing. As an example, a microwave interferometer can be configured with the source of two frequencies for absolute distance measurement, ranging, which is an indispensable requirement of industrial sensing, in addition to velocity measurement. Further applications for millimeter wave interferometric sensors can be considered to overcome the drawback of conventional pulse or FMCW radar in the short-distance ranging, that is hard to achieve high resolution or even impossible to range unless very wide bandwidth is incorporated. Typically, it is difficult to use these conventional techniques in short-distance ranging because of the limit of resolution, that is inversely proportional to the signal bandwidth; these techniques require very short pulse or wide bandwidth, which are difficult in designing the systems to resolve very short time delay. A sole interferometric technique, or FMCW, combined with interferometry is promised to be an ideal solution to compensate for the limitation in short-distance applications, due to high range resolvability, or phase resolvability of interferometry.

The achievements in this research can be extended to radar sensor for automobile, which has a huge potential market in the near future. Recently, millimeter wave radar has been intensively investigated for intelligent cruise control and safety concerns of the vehicle, and most configurations have adopted the FMCW technique. Millimeter wave interferometric operation combined with the FMCW technique is expected to increase the resolution of the radar sensor by the phase-sensitive time domain signal processing in addition to FFT, frequency domain signal processing; and, above all, to solve the conventional short-distance ranging problem of pulse or FMCW radar. Near field

imaging is also one possible application of the sensors reported in this dissertation. Non-destructive material testing and microwave microscopy can be categorized as those of near field imaging. The resolution of near field imaging, especially, relies on the probe dimension, such as the aperture size of an open-ended waveguide or conductor diameter of an open-ended coaxial cable, rather than the operating frequency. Thus, by miniaturizing the probe, it is realizable to achieve high resolution at relatively low operating frequency. Finally, the presented work may be applied for medical and biological purposes, by detecting vital signals from the heart or lungs of human beings or animals through the detected phase using a microwave interferometer. Further recommendation of this application can be envisioned in remote diagnoses by installing the sensor in mobile phones and connecting it through wireless networks, so that vital signals detected are transferred to a doctor in a remote location.

REFERENCES

- [1] A. Kolodziejczyk and M. Sypek, "A.A. Michelson-life and achievements," *Proceedings of SPIE*, vol. 1121, pp.2-14, 8-12 May 1989.
- [2] J.M. Schmitt, "Optical coherence tomography (OCT): A review," *IEEE J. Select. Topics Quantum Electron.*, vol. 5, no. 4, pp. 1205 – 1215, Jul.-Aug. 1999.
- [3] M.M. Gualini, W.A. Kha, W. Sixt, H. Steinbichler, "Recent advancements of optical interferometry applied to medicine," Multi Topic Conference, 2001. IEEE INMIC 2001. Technology for the 21st Century. *Proceedings. IEEE International*, pp. 205 – 211, 28-30 Dec. 2001.
- [4] W.H. Steel, "Another look at the theory of interferometer," *Proceedings of SPIE*, vol. 1121, pp.18-14, 8-12 May 1989.
- [5] W.H. Steel, *Interferometry*. London: Cambridge University Press, 1983.
- [6] R.J. King, *Microwave Homodyne Systems*. London: Peter Peregrinus, 1978.
- [7] J. Musil and F. Zacek, *Microwave Measurements of Complex Permittivity by Free Space Methods and Their Application*. Amsterdam: Elsevier, 1986, Ch. 4.
- [8] C.W. Domier, W.A. Peebles, and N.C. Luhmann, "Millimeter-wave interferometer for measuring plasma electron density," *Rev. Sci. Instrum.*, vol. 59, No.8, pp.1588-1590, 1988.
- [9] X. Liu, W. Clegg, D.F.L. Jenkins and B. Liu, "Polarization interferometer for measuring small displacement," *IEEE Trans. on Instrum. and Meas*, vol. 50, no. 4, pp.868-871, Aug. 2001.
- [10] M. Norgia, S. Donati and D. D'Alessandro, "Interferometric measurements of displacement on a diffusing target by a speckle tracking technique," *IEEE J. Quantum Electron.*, vol. QE-37, no.6, pp. 800-806, Jun. 2001.
- [11] B.G. Zagar, "A Laser-interferometer measuring displacement with nanometer resolution," *IEEE Trans. on Instrum. and Meas*, vol. 43, no.2, pp. 332- 336, Apr. 1994.
- [12] K. Itoh, "Analysis of the phase unwrapping problem," *Applied Optics*, vol. 21, No.14, pp. 2470, July 15, 1982.

- [13] D.C. Ghiglia and M.D. Pritt, *Two-Dimensional Phase Unwrapping Theory, Algorithms, and Software*. New York: John Wiley & Sons, 1998, Ch. 1.
- [14] A.V. Oppenheim and R. W. Schaffer, *Digital Signal Processing*. Englewood Cliffs, NJ: Prentice-Hall, 1975, Ch.10.6.
- [15] *IE3D, Version 10.15*, Zeland Software, Inc., Fremont, California.
- [16] S.J. Goldman, *Phase Noise Analysis in Radar Systems Using Personal Computers*. New York: John Wiley & Sons, 1989, Ch. 10.
- [17] F.E. Churchill, G.W. Ogar, and B.J. Thompson, "The correction of I and Q errors in a coherent processors," *IEEE Trans. Aerosp. Electron. Syst.*, AES-17, no.1, Nov. 1981, pp.131-137.
- [18] D.E. Noon, "Wide band quadrature error correction (using SVD) for stepped-frequency radar receivers," *IEEE Trans. Aerosp. Electron. Syst.*, AES-35, no.6, Oct. 1999, pp.1444-1449.
- [19] R.A. Monzingo and S.P. Au, "Evaluation of image response signal power resulting from I-Q channel imbalance," *IEEE Trans. Aerosp. Electron. Syst.*, AES-23, no.2, Mar. 1987, pp.285-287.
- [20] *33-43GHz GaAs MMIC Image Rejection Balanced Mixer*, AM038R1-00, Data Sheet, Alpha Industries, Inc.
- [21] J. Otto, "Radar applications in level measurement, distance measurement and nondestructive material testing," *Microwave Conference and Exhibition, 27th European*, vol. 2 , pp. 1113 – 1121, Sep. 1997.
- [22] R. Zoughi, *Microwave Non-Destructive Testing and Evaluation*. Boston: Kluwer Academic, 2000.
- [23] M. A. Heald, C. B. Wharton, *Plasma Diagnostics with Microwaves*. New York: John Wiley & Sons, 1965.
- [24] A. Stelzer, C.G. Diskus, K. Lubke, H.W. Thim, "Microwave position sensor with submillimeter accuracy," *IEEE Trans. Microwave Theory Tech.*, vol. 47, no. 12, pp. 2621–2624, Dec.1999.
- [25] A. Benlarbi-Delai, D. Matton, Y. Leroy, "Short-range two-dimension positioning

- by microwave cellular telemetry,” *IEEE Trans. Microwave Theory Tech.*, vol. 42, no. 11, pp. 2056 -2062, Nov. 1994.
- [26] A Benlarbi, J.C Van De Velde, D. Matton, Y. Leroy, “Position, velocity profile measurement of a moving body by microwave interferometry,” *IEEE Trans. Instrum. Meas.*, vol. 39, no. 4, pp. 632-636, Aug. 1990.
- [27] P.E. Engler, S.S. Reisman, C.Y. Ho, “A microwave interferometer as a non contacting cardio-pulmonary monitor,” 1988 Bioengineering Conference, *Proc. of the 1988 Fourteenth Annual Northeast*, pp. 62-65, 10-11 March 1988.
- [28] A.R. Thompson, J.M. Moran, G. W. Swenson, Jr., *Interferometry and Synthesis in Radio Astronomy*. New York: John Wiley & Sons, 1986.
- [29] W. B. Doriese, “A 145-GHz Interferometer for Measuring the Anisotropy of the Cosmic Microwave background,” Ph.D. dissertation, Physics Department, Princeton University, Princeton, New Jersey, 2002.
- [30] G. Franceschetti and R. Lanari, *Synthetic Aperture Radar Processing*. New York: CRC press, 1999, Ch. 4.
- [31] W. F. Feltz, H. B. Howell, R. O. Knuteson, H. M. Woolf, and H E. Revercomb, “Near continuous profiling of temperature, moisture, and atmospheric stability using the atmospheric emitted radiance interferometer (AERI),” *J. Appl. Meteor.*, vol. 42, pp. 584-597, 2003.
- [32] E. N. Ivanov, M. E. Tobar, R. A. Woode, “Microwave interferometry: Application to precision measurements and noise reduction techniques,” *IEEE Trans. Ultrason., Ferroelect., Freq. Contr.*, vol. 45, no. 6, pp. 1526 – 1536, Nov. 1998.
- [33] S. Kim and C. Nguyen, “A displacement measurement technique using millimeter-wave interferometry,” *IEEE Trans. Microwave Theory Tech.*, vol. 51, no. 6, pp. 1724 -1728, June 2003.
- [34] S. Kim and C. Nguyen, “Millimeter-wave Doppler velocimetry for low-velocity measurement,” Accepted for *IEEE MTT-S Int. Microwave Symp. Digest*, June 2004.

- [35] H. H. Meinel, "Commercial applications of millimeter waves history, present status, and future trends," *IEEE Trans. Microwave Theory Tech.*, vol. 43, no. 7, pp. 1639-1653, July 1995.
- [36] M. Wollitzer, J. Buechler, J.F. Luy, U. Siart, E. Schmidhammer, J. Detlefsen, M. Esslinger, "Multifunctional radar sensor for automotive application," *IEEE Trans. Microwave Theory Tech.*, vol. 46, no. 5, pp. 701 -708, May 1998.
- [37] R.H. Rasshofer, E.M. Biebl, "Advanced millimeterwave speed sensing system based on low-cost active integrated antennas," *IEEE MTT-S Int. Microwave Symp. Dig.*, vol.1, pp. 285 –288, June 1999.
- [38] I. Gresham, N. Jain, T. Budka, A. Alexanian, N. Kinayman, B. Ziegner, S. Brown, P. Staecker, "A compact manufacturable 76-77-GHz radar module for commercial ACC applications," *IEEE Trans. Microwave Theory Tech.*, vol. 49, no.1, pp. 44 -58, Jan. 2001.
- [39] N. Weber, S. Moedl, M. Hackner, "A novel signal processing approach for microwave Doppler speed sensing," *IEEE MTT-S Int. Microwave Symp. Dig.*, vol.3, pp. 2233 –2235, June 2002.
- [40] F. Xiao, F.M Ghannouchi, T. Yakabe, "Application of a six-port wave-correlator for a very low velocity measurement using the Doppler effect," *IEEE Trans. Instrum. Meas.*, vol. 52, no.2, pp. 297-301, April 2003.
- [41] W.M. Waters, and B.R. Jarret, "Bandpass signal sampling and coherent detection," *IEEE Trans. Aerosp. Electron. Syst.*, AES-18, pp.731-736, Nov. 1982.
- [42] D.W. Rice, and K. H. Wu, "Quadrature sampling with high dynamic range," *IEEE Trans. Aerosp. Electron. Syst.*, AES-18, pp.736-739, Nov. 1982.
- [43] V. Considine, "Digital complex sampling," *Electronics Letters*, vol. 19, no.16, pp. 608-609, Aug. 1983.

- [44] C. R. Rader, "A simple method for sampling in-phase and quadrature composition," *IEEE Trans. Aerosp. Electron. Syst.*, vol. 20, no. 6, pp. 821-824, Nov. 1984.
- [45] H. Liu, A. Ghafoor, P.H. Stockmann, "A new quadrature sampling and processing approach," *IEEE Trans. Aerosp. Electron. Syst.*, AES-25, no. 5, pp. 733-748, Sep. 1989.
- [46] G. A. F. Seber and A. J. Lee, *Linear Regression Analysis*. New York: J. Wiley & Sons, 2003.
- [47] S. A. Tretter, "Estimating the frequency of a noisy sinusoid by linear regression," *IEEE Trans. Inform. Theory*, vol. IT-31, pp. 832-835, Nov. 1985.
- [48] C.D, Cain, A. Yardim, E. T. Katsaros, "Performance of an FIR filter-based spectral centroid tracker for Doppler determination," *IEEE International Symposium on Circuits and Systems*, vol.5, pp. 2455 – 2458, 11-14 June 1991.
- [49] G. H. Golub and C.F. Van Loan, *Matrix Computation*. Baltimore, MD: The John Hopkins University Press, 1989, Ch. 8.
- [50] J. Salz, "Coherent lightwave communications," *AT & T Tech J.*, vol.64, no.10, pp. 2153-2209, Dec.1985.
- [51] J. R. Barry and E.A. Lee, "Performance of coherent optical receivers," *Proc. IEEE*, vol. 78, no. 8, pp. 1369-1394, Aug. 1990.
- [52] A. Papoulis, *Probability, Random Variables, and Stochastic Processes*. New York: McGraw-Hill, 1984.
- [53] H. Taub and D. L. Schilling, *Principles of Communication Systems*. New York: McGraw-Hill, 1971.
- [54] *HP-ADS, Version 1.5*, Agilent Eesof EDA, Westlake Village, CA.
- [55] J.A. Barnes, A.R. Chi, L.S. Cutler, D.J. Healey, D.B. Leeson, T.E. Mcgunigal, J.A. Mullen, Jr., W.L. Smith, R.L. Sydnor, R.F.C. Vessot, G.M.R. Winkler, "Characterization of frequency stability," *IEEE Trans. Instrum. Meas.*, vol. 20, no. 2, pp. 105-120, May 1971.

- [56] W.P. Robins, *Phase Noise in Signal Sources*. London: Peter Peregrinus, 1998.
Ch. 3.
- [57] J. Rutman, "Characterization of phase and frequency instability in precision frequency sources: Fifteen years of progress," *Proc. of the IEEE*, vol.66, no. 9, pp.1048 – 1075, Sep. 1978.
- [58] J. R. Ashley, T. A. Barley, G. J. Rast, "The measurement of noise in microwave transmitters," *IEEE Trans. Microwave Theory Tech.*, vol. 25, no. 4, pp. 294-318, April 1977.

VITA

Seoktae Kim received the B.S. of electrical engineering degree from Inha University, South Korea in 1989 and M.S. of electrical engineering degree from Pohang University of Science and Technology (POSTECH), South Korea in 1991.

From 1991 to 1998, he was with the Semiconductor Division, Samsung Electronics Co., South Korea, where he was involved with research and development of GaAs electronic devices and Thin Film Transistor Liquid Crystal Display (TFT LCD). He holds four US patents. He received an Honorable Mention Award in the Student Paper Competition of 2004 IEEE MTT-S International Microwave Symposium. His current research interest is millimeter wave radar sensor design for industrial sensing applications.

His permanent address is:

Jowon-Dong 519-29, Jangan-Gu
Suwon, Kyounggi-Do
S. Korea 440-845